Thermal Processing and Microwave Processing of Mixed-Oxide Thin Films

by

Mandar Gadre

A Dissertation Presented in Partial Fulfillment
of the Requirements for the Degree
Doctor of Philosophy

Approved July 2011 by the
Graduate Supervisory Committee:

Terry L. Alford, Chair
David Theodore
Stephen Krause
Dieter Schroder

ARIZONA STATE UNIVERSITY

August 2011

ABSTRACT

Amorphous oxide semiconductors are promising new materials for various optoelectronic applications. In this study, improved electrical and optical properties upon thermal and microwave processing of mixed-oxide semiconductors are reported. First, arsenic-doped silicon was used as a model system to understand susceptor-assisted microwave annealing. Mixed oxide semiconductor films of indium zinc oxide (IZO) and indium gallium zinc oxide (IGZO) were deposited by room-temperature RF sputtering on flexible polymer substrates. Thermal annealing in different environments - air, vacuum and oxygen was done. Electrical and optical characterization was carried out before and after annealing. The degree of reversal in the degradation in electrical properties of the thin films upon annealing in oxygen was assessed by subjecting samples to subsequent vacuum anneals. To further increase the conductivity of the IGZO films, Ag layers of various thicknesses were embedded between two IGZO layers. Optical performance of the multilayer structures was improved by susceptor-assisted microwave annealing and furnace-annealing in oxygen environment without compromising on their electrical conductivity. The post-processing of the films in different environments was used to develop an understanding of mechanisms of carrier generation, transport and optical absorption. This study establishes IGZO as a viable transparent conductor, which can be deposited at room-temperature and processed by thermal and microwave annealing to improve electrical and optical performance for applications in flexible electronics and optoelectronics.

Dedicated to my family:

Madhuri Gadre, Jayram Gadre, Milind Gadre and Amruta Bedekar.

ACKNOWLEDGMENTS

It is a privilege to express my deep gratitude towards all those who have made this dissertation possible.

First and foremost, I thank my research advisor Prof. Terry Alford. He has been a great guide and a mentor to me, and a constant source of encouragement and support. I have thoroughly enjoyed my interactions with him, and learned a great deal while working on various research projects as his student. I am and will always be grateful to him for giving me the opportunity to work with him.

I would also like to thank all my committee members for their support and guidance: Prof. Dieter Schroder, Prof. Stephen Krause and Dr. David Theodore.

I thank Tim Karcher for the training and inputs about the sputtering system. I acknowledge the help of Barry Wilkens, David Wright, Emmanuel Soignard, Christian Poweleit, Kenneth Mossman and Diana Convey, for the training and usage of various instruments.

Words will never be enough while I express my joy of having worked with, and the gratitude in my heart towards my labmates Karthik Sivaramakrishnan, Anil Indluru, Rajitha Vemuri, Sayantan Das, Mohammad Kabiri and Aritra Dhar. They have helped me with various discussions and experiments and have been a terrific group of graduate students to be with.

I thank all my friends from ASU, specially Supreet Bose, Srinivas Arepalli, Wilbur Lawrence, Abhishek Kohli, Aritra Dey, Shubhashish Bandopadhyay and Siddharth Gupta for being there to share my joys and sorrows. I am honored to have known fellow materials science graduate students and researchers at ASU, specially Erika Engstrom, Jordan Kennedy, Heather McFelea, John Gustafson, Jeff Thompson, Harsha Kosaraju, Cedric Hurth, Elise Switzer, Sonja Tasic, Billy Mylan, Edward Olaya and Jianing Yang. I thank you all, with all my heart.

I heartily thank my friends from outside ASU. They have been a source of constant support and encouragement, and I will only attempt to name a few here: Purushottam Dixit, Kaustubh Nadkarni, Ameya Bondre, Gayatri Natu, Onkar Dalal, Sanjyot Gindi, Chaitanya Bokil, Makarand Datar, Makarand Joshi, Varun Kanade, Sumedh Risbud, Ishika Sinha, Gireeja Ranade, Saee Keskar and Asmita Halasgikar.

Last but not the least: I will never be able to thank in words those who are my immediate and extended family. My mother Madhuri Gadre, father Jayram Gadre, brother Milind Gadre, fiancée Amruta Bedekar and many more have always been there – to support, encourage and guide me. It is because of their love, that I have been able to achieve anything, if at all.

TABLE OF CONTENTS

Page

Page

Page

LIST OF TABLES

Table Page

LIST OF FIGURES

Figure Page

Page

Page

Page

Chapter 1

INTRODUCTION

1.1 INTERACTION OF MICROWAVES WITH MATTER

Electromagnetic (EM) radiation is a very crucial form of energy available to mankind. It consists of electric and magnetic fields that fluctuate sinusoidally in planes perpendicular to each other and propagate at the speed of light. EM radiation does not need a medium to in which to travel. The dual nature of EM radiation is evident through its wave-like behavior in the case of interference and diffraction and its particle-like behavior in the case of phenomena like the photoelectric effect. The quanta of EM radiation are termed as photons. The frequency ν and the wavelength λ are inversely proportional to each other, related by $\nu = c/\lambda$, where c is the speed of light in vacuum. The energy E of the EM radiation depends linearly on the frequency ν, given by $E = h\nu$ where h is the Planck's constant.

The electromagnetic spectrum is classified into regions of increasing frequencies (or equivalently, energies): radio waves, microwaves, infrared, visible light, ultraviolet, X-rays, and gamma rays. Microwaves are generally taken to have frequencies from 300 MHz to 300 GHz which correspond to wavelengths of 1 m down to 1 mm, respectively. Microwaves have found their application in diverse

fields such as microwave heating, communications, RADAR, electronic warfare, radiation therapy, non-destructive testing of materials, *etc*. [1-1].

The interaction of microwaves with materials takes place through the two components of the microwave radiation: the electric field *E* and the magnetic field *H*. The response of a material when exposed to an electromagnetic radiation may be understood through the dielectric constant ε of the material. The dielectric constant, also known as the permittivity of the material, describes the ability of the material to be polarized in the applied electric field. To understand the dielectric response to sinusoidal fields such as the microwaves, complex permittivity ε^* is employed: $\varepsilon^* = \varepsilon' + i\,\varepsilon''$. The real part of the dielectric constant is a measure of the penetration of microwave energy in the material; while, the imaginary part indicates the ability of the material to store the energy [1-2]. The dielectric properties vary with temperature and frequency. Water, for example, has both high ε' (78.0) and high ε'' (12.0) at 2.45 GHz making it amenable to microwave heating since it allows good penetration as well as good absorption. Alumina has a high ε' (8.9) providing good penetration but low ε'' (0.009) which does not allow any significant absorption. This makes alumina virtually transparent to microwaves at 2.45 GHz and thus a loss-less material. Silicon carbide, which is used in the susceptors employed in the present work,

has high ε' (30.0) and high ε'' (11.0) making it an excellent lossy material for microwave energy absorption.

The interaction of microwaves with materials can be classified into four broad categories [1-1]:

1. Opaque materials: conductive materials with free electrons mostly reflect and do not allow the electromagnetic radiation to penetrate;
2. Transparent materials: low dielectric loss materials or insulating materials like glass and air allow microwaves to pass through without significant attenuation, without much reflection or absorption.
3. Absorbing materials: these materials are termed as lossy dielectrics or high dielectric loss materials which absorb microwave energy and convert it to heat.
4. Magnetic materials: materials like ferrites interact with the magnetic component of the electromagnetic radiation and become heated.

In any given material, various entities such as the free electrons, valence electrons, ions, molecular dipoles, and interfacial charges respond to the applied electric and magnetic field. The sinusoidal fields cause the charged species to polarize and vibrate. Different charged species all have different natural frequencies of vibration. The conversion to heat occurs because of the lag of the

response of the material to the applied electromagnetic field. In the heating of dielectric materials, it is assumed that the magnetic field does not contribute to microwave absorption and the heating occurs entirely due to the electric field [1-1].

There are four principal polarization mechanisms in dielectric solids [1-1]:

a. Electronic polarization: When an atom is subjected to an external electric field, displacement of the electron cloud with respect to the nucleus gives rise to formation of a dipole. Valence electrons shift much more easily than the tightly bound core electrons. Covalent crystals have large dielectric constants owing to the displacement of the valence electrons. Thus, materials like silicon (ε_r'=11.9) and germanium (ε_r'=11.9) have high real components of the dielectric constant; hence, microwaves easily penetrate these materials.
b. Dipole polarization: Under the application of an external electric field, polar molecules orient themselves with the field. The lag associated with this response and the inter-molecular collisions lead to dielectric heating. In some materials, the polarization can be retained due to the need for thermal activation for molecular rotation, which gives rise to the formation of "electrets" [1-1].

c. Ionic or atomic polarization: Relative displacement of the positive and negative ions or atoms within molecules and crystal structures from their equilibrium lattice sites gives rise to ionic polarization.

d. Interfacial polarization: This involves the accumulation of free charges at interfaces located within the material: grain boundaries, phase boundaries and defect regions. Under the application of an electric field, the mobile charges are displaced and accumulated at such interfaces.

The contributions by various polarization mechanisms are dependent on the frequency. Figure 1-1 shows the dependence of loss mechanisms in dielectrics on the frequency of the electromagnetic radiation.

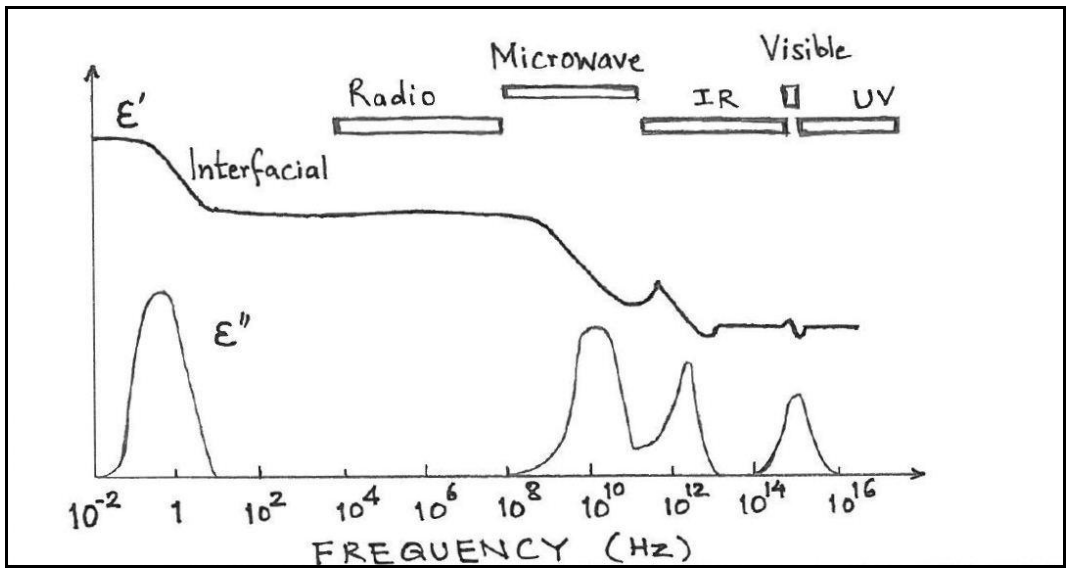

Figure 1-1: Frequency dependence of polarization mechanisms in dielectrics [1-1]

1.2 MICROWAVE PROCESSING OF MATERIALS

Microwave heating of materials has been explored since the 1940's; Clark and Sutton [1-3] and Semenov *et al.* [1-4] provide a review of microwave processing of materials. For many decades, a large part of the work on microwave processing is devoted to dielectric ceramic and glass materials. In the past decade, a growth in the microwave processing of semiconductors and powder metals has been observed. Modern processing practices in the semiconductor industry could benefit greatly from the peculiar characteristics of microwave processing and the advantages it offers.

Contactless, volumetric heating is the key characteristic of microwave processing. In conventional heating, the thermal energy is transferred to the material from the outside to the inside, creating a temperature gradient. Small penetration depth of infrared (less than 0.1 mm) leads to energy deposition being limited to the surface layers [1-4]. Microwave heating overcomes this through absorption of the microwave energy throughout the volume of the material. Since the surface loses energy by radiation, the core of the material is usually hotter and the temperature profile is the inverse of that seen in conventional heating. Volumetric heating has the advantage of uniform and rapid processing of

materials leading to an increased throughput. Rapid heating in semiconductors provides the advantage of minimal diffusion of various species into the substrate.

Poorly absorbing materials (those with small values of ε") can be hard to heat using microwaves. One common solution to this is the use of microwave susceptors to provide hybrid heating. Microwave processing can also be employed for selective heating of materials, which is not possible with conventional heating.

Some barriers to adoption of microwave processing of materials are the inability to prevent unwanted reactions, inaccurate temperature measurements, preventing hotspots and arching, availability and cost of equipment, *etc*.

1.3 MULTICOMPONENT TRANSPARENT CONDUCTING OXIDES

Materials that exhibit optical transparency to visible light as well as reasonable electrical conductivity can be classified into three categories: very thin pure metals, highly doped conjugated organic polymers, and degenerately doped wide band gap oxide or nitride semiconductors [1-5]. These materials have two such properties that are strongly linked to each other. Metals which are highly

conductive do not normally transmit visible light; while, highly transparent materials like oxide glass are insulators. The challenge is to decouple the two properties such that the material maintains its transparency while becoming electrically conductive at room temperature [1-6].

An important figure of merit used to compare transparent conducting materials is given by Haacke [1-8]:

$$\Phi = T^{10}/R_s \tag{1-1}$$

where T is the optical transmittance and R_s is the sheet resistance. If α is the visible absorption coefficient, ρ the resistivity of the material and x is the film thickness, we have

$$T = \exp(-\alpha x) \text{ and } R_s = \rho/x. \tag{1-2}$$

Thus we have an expression for Haacke's figure of merit:

$$\Phi = (\rho/x) \exp(-\alpha x) \tag{1-3}$$

Using this definition the maximum figure of merit for silver is approximately 0.023 Ω^{-1} (using $\alpha = 10^6$ cm^{-1} and $\rho = 1.6\times10^{-6}$ Ω-cm with 1 nm thick film). In comparison, a 1000 nm thick film of indium tin oxide (ITO) has a figure of merit

that is an order of magnitude higher: 0.22 Ω^{-1} using values for $\rho = 1.6\times10^{-4}$ Ω-cm and $\alpha = 10^{-3}$ cm^{-1} [1-5].

Conjugated organic polymers have been reported to have very low resistivities (10^{-5} to 10^{-3} Ω-cm) but suffer from low carrier mobility, low carrier density, and poor transparency. In addition, there are challenges regarding their environmental stability due to sensitivity to oxygen and moisture [1-5].

Thus, the universal choice for electrode applications requiring transparency and low sheet resistance are the transparent conducting oxides (TCOs). TCOs can be divided into two categories based on their constituents: single-component systems (*e.g.*, zinc oxide, tin oxide) and multi-component systems like indium-tin oxide, indium-zinc oxide (IZO), and indium-gallium-zinc oxide. Indium-oxide based materials are currently used in the vast majority of high-performance display applications [1-5].

The primary consideration in the selection of a TCO material for use with any class of substrate is the ability to deposit material with adequate optical and electrical properties. If polymeric substrates are used, additional constraints on processing parameters are encountered. Polymer substrates are heat-sensitive,

and suffer from dimensional and structural instability when exposed to various solvents or energetic radiation [1-6].

An important material requirement is that the mechanisms for doping the wide band gap oxide can be activated at low process temperatures and are operational even in the disordered amorphous state [1-5]. Amorphous ITO undergoes crystallization at low annealing temperatures and can be deposited in crystalline form by heating the substrates to 150-200 ^{o}C. Crystalline IZO can be achieved by depositing the films at elevated substrate temperatures (~350 ^{o}C) or annealing post-deposition at around 500 ^{o}C. The amorphous nature of IZO, unless at elevated temperatures, is due to the immiscibility of ZnO and In_2O_3. The two components must undergo phase separation to allow crystallization. The kinetics of the phase separation are slow and thus Zn has the effect of stabilizing the amorphous structure [1-5]. In more complex systems like a-IGZO, it is expected that some alloy combinations will be more stable than other combinations. The remarkable feature of these materials is that while they do not have extremely high electron mobilities in crystalline form, the electron mobility remains nearly unchanged even as the atomic disorder is increased in polycrystalline and amorphous forms. Even when the material is truly amorphous the electron mobility can be more than an order of magnitude higher (10–50 $cm^2 V^{-1} s^{-1}$) than conventional amorphous materials, which have electron mobilities

<1 $cm^2 V^{-1} s^{-1}$. The origin of the high mobility has been attributed to the high degree of overlap of the spherically symmetric cation orbitals that make up the conduction band [1-9].

As categorized by Hosono [1-10], amorphous oxides based on post-transition metals fall in the category of ionic and wide band-gap semiconductors, unlike amorphous silicon (a-Si) which is a covalent narrow band-gap semiconductor. Hosono also notes that in amorphous materials in general, the structural randomness is mainly contributed by the energetically weak part, which is the bond angle distribution in case of the amorphous oxide semiconductors. The effective mass of the electron, which essentially corresponds to the transfer rate between neighboring cation s-orbitals, depends on how wide the bond-angle distribution is [1-10]. Hosono considers the difference between covalent amorphous semiconductors like a-Si and amorphous TCOs, and notes that in the case of covalent conductors, the overlap between the vacant orbitals of neighboring atoms is largely dependent on the bond angle. This results in the creation of deep localized states at high concentrations affecting the drift mobility. Unlike the covalent amorphous semiconductors, the amorphous oxide semiconductors are characterized by the radius of the metal cation s-orbitals determining the magnitude of the overlap of orbitals. When the spatial spread of the s-orbitals is larger than the inter-cation distance, the magnitude of orbital overlap is largely insensitive to the bond angle variation. This is due to the s-

orbitals being spherical in shape. Thus, the choice of metal cations while fabricating amorphous metal oxide semiconductors is very crucial. Heavy post-transition metal atoms like gallium which have large ionic radii help in achieving large orbital overlap leading to the high values of mobilities seen in the oxide semiconductors. As a result, the properties of crystalline and amorphous oxide semiconductors are much more similar than what is typically observed in the case of amorphous and crystalline phases of other elemental and compound semiconductors.

Nomura *et. al.* [1-11] have employed computer simulations with Extended X-Ray Absorption Fine Structure (EXAFS) analysis to investigate amorphous structure of amorphous IGZO. The average coordination numbers for In, Ga and Zn atoms by the oxygen atoms are seen to be >5, ~5 and ~4, respectively. The distinguishing feature of a-IGZO is the peculiar coordination number of indium, which is the combination of 5- and 6-coordination sites. This is unlike crystalline IGZO which contains only 6-coordinate indium atoms. The 5% lower density of the amorphous phase has been attributed to this difference in the coordination observed in the two states. Yaglioglu [1-12] have concluded from their studies on amorphous IZO films that in a change in volume occurs due to the the annihilation or creation of oxygen vacancies during annealing. Moreover, relaxation of the amorphous phase is also observed regardless of the ambient.

1.4 CHAPTER OUTLINES

Following the introduction in Ch. 1, Ch. 2 describes the work on microwave processing of arsenic-doped silicon. An attempt is made to probe into and understand the mechanism of microwave annealing of doped silicon. Shorter processing times have been achieved with susceptor-assisted microwave heating of the ion-implanted silicon. Ceramic composite susceptors, made of alumina and silicon carbide (SiC), have been used to achieve the required temperatures for repairing the lattice damage caused by As doping and for the electrical activation of the As dopants.

Chapter 3 describes the work on amorphous indium-zinc oxide (a-IZO) thin films deposited on a flexible polymer substrate polyethylene naphthalate (PEN). Complete electrical and optical characterization of the a-IZO thin films is presented, along with the effect of annealing in different ambient environments on the electrical and optical properties. Through this effort, an attempt to better understand the mechanism of carrier-generation in amorphous thin films is made. This is very crucial in the light of processing constraints imposed by the organic polymer substrates used which do not allow high temperatures. The effect of low-temperature anneals in air, oxygen, and vacuum on the properties of amorphous indium-zinc oxide thin films grown on polyethylene naphthalate (PEN) is studied.

Electrical, optical and surface characterization was carried out before and after annealing. An approximately 62-fold increase in the Haacke figure of merit was achieved by annealing the films in air at 150 ºC for 6 hrs. The difference in electrical performance of films annealed in different environments indicated the role of oxygen vacancies in electrical conduction. The degradation in electrical properties upon annealing in oxygen was achieved by subjecting the films to a subsequent vacuum anneal. A model for electron scattering was used to compare the measured and calculated values of carrier mobility and it showed that the mobility was influenced by structural defects at low carrier concentrations (1-4×10^{18} cm^{-3}).

Chapter 4 elucidates the obtainment of a-IGZO thin films of the highest transmittance reported in literature. The films were deposited onto flexible polymer substrates at room temperature employing RF sputtering. The films were annealed in vacuum, air, and oxygen to enhance electrical and optical performance. Electrical and optical characterization was done before and after annealing. A partial reversal of the degradation in electrical properties upon annealing in oxygen was achieved by subjecting the films to subsequent vacuum anneal. A model based on film texture and structural defects which showed close agreement between the measured and calculated carrier mobility values.

Chapter 5 reports fabrication, characterization and processing of high conductivity IGZO/Ag/IGZO multilayer structures with high transmittance. For multilayers with 7 nm Ag layer, the carrier concentration was 1×10^{22} cm^{-3} and resistivity was 6.7×10^{-5} Ω cm, while still achieving T_{avg} at 87%, resulting in FOM of 1.7×10^{-2} Ω^{-1}. Low resistivity and high T_{avg} were obtained when the Ag layer thickness corresponds to the initial formation of a continuous metal layer. The multilayers were subsequently microwave-annealed which resulted in decrease in the oxygen vacancy concentration thereby reducing the free carrier absorption and improving the T_{avg}. This was confirmed by furnace-annealing the films in oxygen environment. The difference in the extent of improvement in the optical transmission upon annealing by the two methods was explained by the longer duration of oxygen anneals.

The complete work is summarized and future work is detailed in Ch. 6. For the microwave processing of materials – both covalent semiconductors like silicon and amorphous transparent conducting oxides like IGZO, it may be attempted to process samples of bigger sizes. This may be used for investigating into any non-uniformities resulting from the microwave anneals. Moreover, use of multiple-frequency microwave cavity applicators may be employed to obtain better uniformity and possibly to further hasten the processing. In this study, the microwave anneals have been carried out in ambient conditions. Various other

environments like inert gases (e.g. argon), oxidizing environments (e.g. oxygen) and reducing environments (e.g. forming gas) may be used and their effect studied on the properties of materials being processed.

The effect of deposition conditions and annealing IGZO thin films on the emissivity of the films may be studied and their emissivities compared to the existing commercial low-emissivity (*'low-e'*) coatings available. For the IGZO/metal/IGZO multilayer structures, different metals may be tried and their relative electrical and optical performance may be studied. Some choices for the metal layer are gold and copper. Deposition of IGZO thin films may also be tried by a sol-gel route and its stability and manufacturability compared with the RF sputtering at room temperature. Also, mechanical properties of the IGZO thin films on flexible polymer substrates like PEN and PET may be studied and compared, along with the investigation into their robustness to humidity. Temperature and humidity-controlled chambers (T&H chambers) may be used for the same.

Chapter 2

DOPANT ACTIVATION IN AS IMPLANTED SI BY SUSCEPTOR-ASSISTED MICROWAVE ANNEALING

I. INTRODUCTION

For more than four decades, silicon device features have been rapidly scaled down, driven by the requirements stated in the International Technology Roadmap for Semiconductors (ITRS). According to the roadmap, physical gate lengths will need to be reduced to 13 nm by 2013, with corresponding junction depths of less than 9 nm [2-1]. While faster device performance can be achieved by reduction of critical dimensions, the scaling down presents various processing challenges. For example, as junction depths decrease the contact resistance increases resulting in increased power dissipation [2-2]. Significant increases in dopant concentration are needed to offset the effects of the scaling down of device features. The most commonly used method for the introduction of dopant atoms is ion implantation. Concentrations of implanted atoms exceeding 10^{20} cm^{-3} are already used in production today [2-3]. Increasing the doping concentration alone is not sufficient; high doping along with electrical activation of the dopant atoms ensures a decrease in resistivity of the doped silicon and thereby a reduction of the contact resistance [2-4].

The implantation of high concentrations of dopants into the silicon results in a highly damaged silicon surface layer, especially when implanting heavy atoms such as arsenic. The depth of the damaged layer is directly proportional to the energy of the implanted dopant and could even extend well past the intended junction depth of the device region [2-4]. Large amounts of lattice damage result in increased sheet resistance. High temperature anneals are performed to repair the damage created during ion implantation and to activate the implanted dopants electrically [2-5]. The high temperature used for such processing gives rise to complications such as significant diffusion of dopant atoms. Both vertical and lateral diffusion of dopant atoms can degrade device performance [2-2]. Rapid thermal processing (RTP) has been used to reduce the diffusion of dopants during annealing with the most common methods being lamp and laser annealing [2-6]. Both lamp and laser annealing can achieve the temperatures needed to repair a disordered silicon lattice and activate the dopant atoms. However, a shortcoming of both of these methods is the uneven heating caused by two factors: the difference in emissivities of the various near-surface device materials and the photons used in lamp and laser heating not penetrating beyond the surface regions of silicon [2-6,7].

Microwave heating has been presented as a possible alternative to other RTP methods in silicon processing [2-7 - 2-10]. Thompson *et al.* have reported the

benefits of microwave heating for solid state reactions in silicon (*i.e.*, silicide formation and Si layer exfoliation in H ion implanted Si) [2-11,12]. Microwave heating of silicon allows for more even, volumetric heating of the wafer due to the greater penetration depth of microwave radiation. Rapid uniform microwave heating at relatively lower temperatures may result in less dopant diffusion [2-10]. Alford *et al.* have used microwave processing to study the comparative effects of microwave heating on highly damaged layers of boron and arsenic ion-implanted silicon [2-13]. In the present study, shorter processing times have been achieved with susceptor-assisted microwave heating of the ion-implanted silicon. Ceramic composite susceptors, made of alumina and silicon carbide (SiC), have been used to achieve the required temperatures for repairing the lattice damage caused by As doping and for electrical activation of the As dopants. Such susceptor-assisted microwave annealing helps reduce the processing times to 100 s. Microwave initiation of solid phase epitaxial re-growth (SPEG) is observed. Dopant activation and SPEG can take place in silicon at temperatures as low as 500 ^{o}C. In this paper we discuss the motivation for using the composite susceptors and the advantages of microwave annealing such as reduced processing time and near-complete electrical activation of the dopants without allowing extensive dopant diffusion into the Si substrate.

II. EXPERIMENTAL

Substrates used in this work consisted of *p*-type Arsenic doped (100) orientated silicon wafers that were cleaned using a Radio Corporation of America procedure. The cleaned silicon wafers were placed in an Eaton Nova NV10-180 batch process ion implanter. Selected wafers were implanted at room temperature with two different arsenic ion energies and two different dosages: 30 keV and 180 keV, 0.5×10^{15} cm^{-2} and 1×10^{15} cm^{-2}, respectively. To minimize ion channeling, all wafers were oriented with their surface normal 7^{o} from the incident beam, and with a 45^{o} in plane twist. Wafer heating was minimized by coating the wafer backs with a thermal conductive paste prior to loading the wafers.

Microwave anneals of the arsenic implanted silicon were performed in a single-frequency (2.45 GHz), 2.8×10^{4} cm^{3} cavity applicator microwave system equipped with a 1300 W magnetron source. Silicon carbide coated alumina susceptor (SiC-Al_2O_3) microwave susceptors were used to obtain temperatures needed for dopant activation and SPEG and to enable uniform heating. Microwave susceptors have been shown as a viable alternative to primary microwave heating, especially in materials which do not absorb much more microwave power at lower temperatures [2-12]. For this work the susceptor was placed below the implanted

silicon substrate in order to achieve higher surface temperatures, which ranged 620–720 ^{o}C depending on process time.

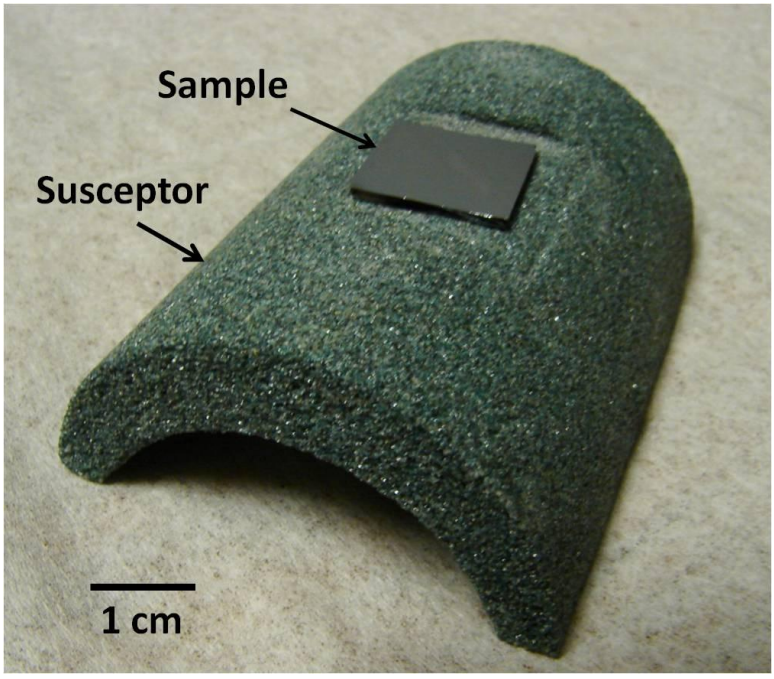

Fig. 2-1. Experimental setup showing the susceptor and the sample.

Figure 1 shows the experimental setup with the susceptor and sample. The silicon carbide susceptor contained silicon carbide particles dispersed in an alumina matrix. The cylindrical shell of the susceptor was cut in half. A stage the size of the implanted samples (1cm×1cm) was cut on the convex side of the semi-cylindrical piece of the susceptor. The depth of the stage was kept the same as the thickness of the implanted sample. The flat stage, as opposed to the curved surface, promotes uniform heat transfer from the susceptor to the sample.

Anneal times ranged from 40 to 100 s. A Raytek Compact MID series pyrometer with a spectral response of about 3.9 μm (with a temperature range of 200 to 1200 ºC) was used to monitor the near surface temperature. The pyrometer was set for the emissivity of Si (0.7), which depends on the wavelength used, the material's dielectric parameters, and the temperature range [2-14].

Figure 2-2 shows a typical plot of surface temperature versus anneal time for a 1×10^{15} As^{+} cm^{-2} sample during microwave annealing, with and without using a susceptor. The anneal time is defined as the duration between when the microwave is switched on and when the microwave is turned off. Once the microwave was turned off, the cavity was opened and a Type-K thermocouple was brought into contact with the sample surface. The readings from the pyrometer and the thermocouple were compared and found to be within 10 ºC of each other. Un-assisted microwave anneals (without a susceptor) were also carried out on the samples. In this case, the surface temperatures were observed to be under 100 ºC for similar anneal times.

Samples were characterized prior to, and after microwave annealing. Implant damage was quantified by Rutherford backscattering spectrometry (RBS) and ion channeling using a 2.0 MeV He^{+} analyzing beam. Samples were analyzed in

random and [001] channeled orientations. Helium ions were collected using a solid state detector, positioned 13^{o} from the incident beam. The software program RUMP was used to simulate damaged-layer thicknesses and ion dose[15]. Secondary ion mass spectroscopy (SIMS) was done with a Cameca IMS 3f magnetic-sector tool to study and compare depth profiles of the un-annealed and microwave-annealed samples. The SIMS analysis utilized O_2^+ as the primary ions with an impact energy of 12.5 keV and 60 nA ion current. Inspection of the microstructure was done using cross-section transmission electron microscopy (XTEM) using a Philips CM200-FEG TEM at an operating voltage of 200 kV. Defect contrast was enhanced using 220 bright-field and dark-field imaging. TEM samples were prepared using a FEI835 focused-ion beam tool with a gallium ion-source.

To monitor dopant activation, sample surfaces were contacted with an in-line four-point-probe equipped with a 100 mA Keithley 2700 digital multimeter. To determine carrier concentration and mobility after microwave processing, Hall-effect analysis was performed using an Ecopia HMS-3000 Hall effect measurement system. Samples were mounted to printed circuit boards using silver paint.

III. RESULTS

Arsenic implanted silicon samples were annealed with microwaves to study the extent to which the damage caused by ion implantation can be repaired. With the use of the susceptor, Si surface temperatures as high as 720 ºC were achieved with only a 100 s microwave anneal. In comparison, the temperatures achieved without susceptors were below 100 ºC, as shown in Fig. 2. The average heating rate was observed to be the same for both medium and high dose samples (5×10^{14} As^{+} cm^{-2} and 1×10^{15} As^{+} cm^{-2}) and for both of the implant ion energies (30 keV and 180 keV). Duplicate anneals were done in which the wafers resided on the silicon carbide susceptor with the implanted surface layer face-up in some cases and for other cases with the implanted surface face-down. There was no significant difference in the surface temperatures recorded.

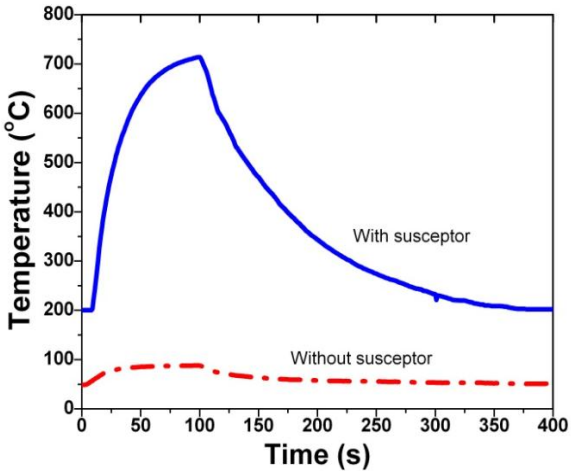

Fig. 2-2: Plot depicting typical surface temperatures of the implanted wafers (monitored by a pyrometer) as a function of time during microwave annealing.

Table 2-1.Sheet Resistance and Hall-effect measurements along with the calculated microwave skin depth obtained from implanted silicon prior to and after 40 s of microwave annealing. The skin depth is calculated at 2.54 GHz.

Implant description	Sheet Resistance (Ω/sq)	Mobility (cm^2/V.s)	Concentration (cm^{-3})	Skin depth (μm)
30 keV, 5×10^{14} As^+ cm^{-2}	1.11×10^2	63.50	4.22×10^{19}	532
30 keV, 1×10^{15} As^+ cm^{-2}	9.9×10^2	53.14	8.37×10^{19}	338
180 keV, 1×10^{15} As^+ cm^{-2}	4.66×10^1	64.66	9.96×10^{19}	1012

Before microwave anneals, all of the sheet resistance and Hall conductivity values were out of range on the respective instruments. Table I shows the results of Hall measurements done on the As^+ implanted Si wafers microwave annealed for 40 s. For each of these measurements, the Ohmic character of the contact between the silver paint and the surface layer was tested. The skin depth was calculated for microwaves at the frequency 2.45 GHz which is used in the single-frequency microwave cavity applicator.

Figure 2-3 displays the results of ion channeling analysis of silicon samples implanted with 30 keV, 1×10^{15} As^+ cm^{-2} prior to and after microwave processing

using microwave susceptors. Spectrum (*a*) in Fig. 2-3 corresponds to the randomly oriented RBS spectrum for arsenic implanted silicon, spectrum (*b*) corresponds to as-implanted samples oriented in a [001] channeled direction, and spectrum (c) correspond to the [001] ion-channeled spectrum for arsenic implanted after the microwave anneal.

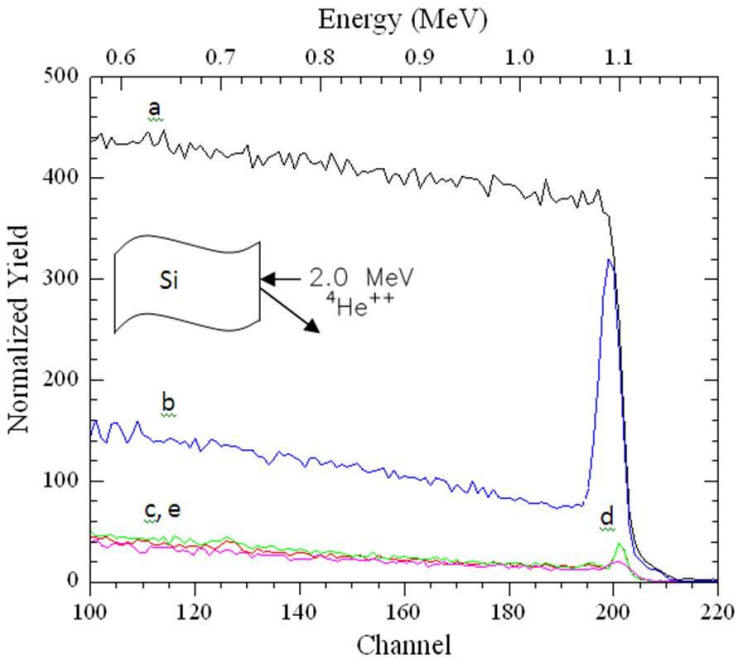

Fig. 2-3: Backscattering spectra from 1×10^{15} As^{+} cm^{-2} : (*a*) as-implanted Si in the random orientation, (*b*) in a [001] channeled direction, (*c*) post 40 s anneal in a [001] channeled direction, (*d*) post 70 s anneal in a [001] channeled direction, and (*e*) virgin silicon in a [001] channeled direction.

As can be seen in spectrum (b), an implant dose of 1×10^{15} As^{+} cm^{-2} is sufficient to produce a thin amorphous silicon layer at the surface of the implanted samples. Previous research has shown that the threshold dose for amorphization[15] of the

silicon with arsenic implantation is approximately 2×10^{15} As^{+} cm^{-2}. RUMP simulation of spectra (b) in Fig. 2-3, determined the amorphous layer thickness to be 50 nm - approximately twice the projected range of 26.2 nm for 30 keV As^{+} ions implanted into Si[15]. Spectrum (c) in Fig. 2-3 demonstrates that after 70 s of microwave processing, nearly all of the implant-induced damage in the arsenic implanted silicon has been removed. Comparison of spectrum (c) with the channeled spectrum (e) of virgin silicon reveals that the two spectra coincide. Normalized yield comparison or χ_{min} is the ratio of the aligned yield to the random yield. Normalized yield comparison between spectrum (c) and (a) gave a χ_{min} value of 0.04 while the χ_{min} value for unimplanted silicon was 0.03, indicating more than 95% As^{+} on silicon sites. Figure 2-4 depicts the variation of %As in Si sites and the corresponding conductivity achieved with increasing microwave annealing time for Si doped with 30 keV 1×10^{15} As^{+} cm^{-2}. The normalized yield of arsenic implanted samples did not decrease further with increasing anneal time to 100 s.

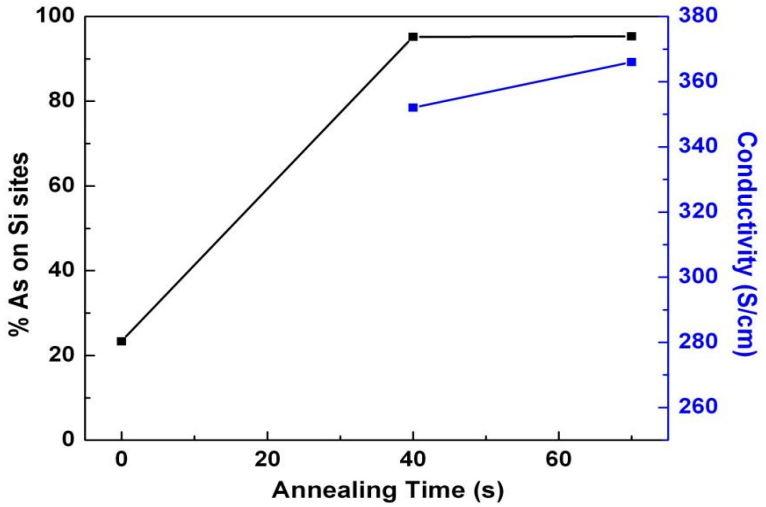

Fig. 2-4: Plot showing the variation of %As in Si sites and the corresponding conductivity achieved with increasing microwave annealing time for Si doped with 30 keV 1×10^{15} As cm^{-2}.

Sheet resistance was monitored between microwave anneals to determine the extent of dopant activation. The change in sheet resistance (R_s) during successive microwave anneals for the three types of implanted silicon samples is depicted in Fig. 2-5. As can be seen in the figure, samples implanted with arsenic doses ranging $0.5–1\times10^{15}$ cm^{-2} show that R_s of the implanted silicon falls dramatically within 40 s of microwave processing. Also, R_s nearly saturates for all microwave processing longer than 40 s. Increasing implant dose corresponds to a decrease in the saturation value of R_s, an expected result if dopant activation occurs during microwave processing [2-2, 4]. This effect is indicative of arsenic activation in *n*-type silicon. For a higher arsenic implant dose, the sheet resistance of implanted samples saturates at a lower value when the implanted arsenic is electrically

activated [2-2, 4]. Backscattering spectra similar to those in Fig. 2-3 confirm that processing beyond the saturation time has little effect on damage repair in arsenic implanted silicon samples.

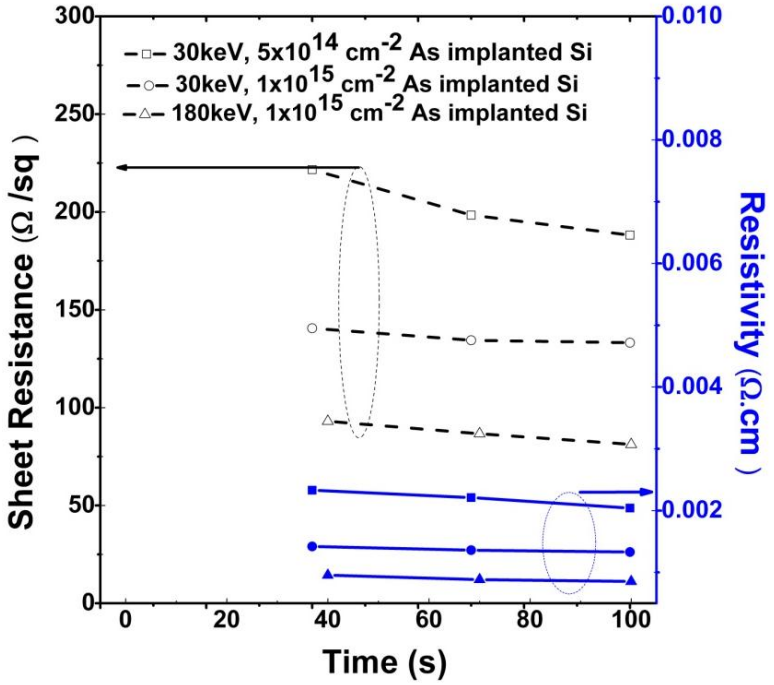

Fig. 2-5: Sheet resistance R_s and resistivity as a function of microwave time for Si implanted with (■ – 30 keV 5×10^{14} cm^{-2}, ● – 30 keV 1×10^{15} cm^{-2}, and ▲– 180 keV 1×10^{15} cm^{-2}) As^+ and microwave annealed for 40, 70, and 100 s.

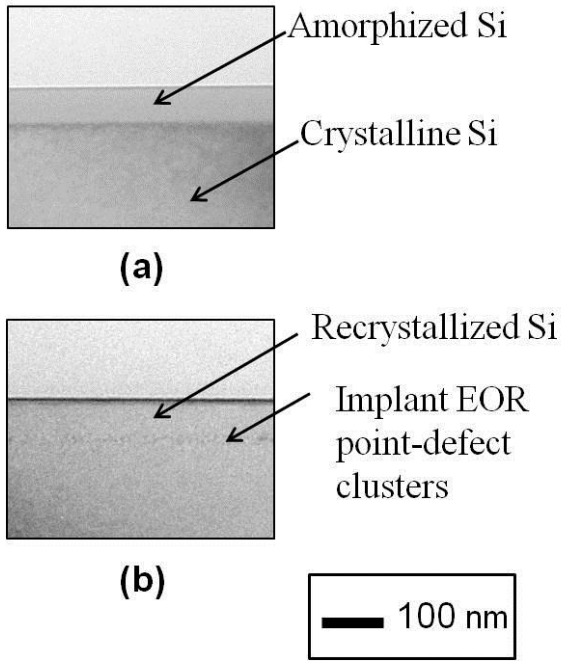

Fig. 2-6: XTEM images of Si implanted with 30 keV, 1×10^{15} As^{+} cm^{-2}: (*a*) as-implanted and (*b*) after 40 s microwave annealing

In order to view the extent of microwave-induced recrystallization in ion-implanted silicon, XTEM was performed on arsenic implanted and microwave annealed silicon samples. Figure 2-6 presents the results of XTEM analysis. The as-implanted samples contain an amorphous layer at the surface of the sample. The amorphous region is visible as the lightly shaded area in Fig. 2-6a. Figure 2-6b demonstrates the effect of microwave processing of the sample pictured in Fig. 2-6a for 40 s. The XTEM micrograph shows that the amorphized Si has recrystallized, but with a small band of defects. Further microwave processing of arsenic implanted silicon samples resulted in XTEM micrographs (not shown) which demonstrated a diminishment of the defect bands shown in Fig. 2-6b.

Although Fig. 2-5 demonstrates that dopant activation occurs during microwave processing, it does not indicate the extent of dopant activation. Hall effect results shown in Table I show the extent of dopant activation by displaying the resultant carrier concentrations. Combined with Fig. 2-5, these results show that the samples experienced near complete electrical activation with microwave annealing. Figure 2-7 depicts the SIMS profiles of arsenic dopants in the as-implanted and microwave-annealed samples. As can be deduced from the figure, microwave anneals are able to repair the damage resulting from the ion implantation and also activate the dopants without significantly allowing them to diffuse deeper into the silicon substrate. This is a crucial requirement for modern annealing techniques where a high degree of diffusion of dopants into the substrate could result in reduced gate lengths and punch-through in channel regions of transistors [2-2,4].

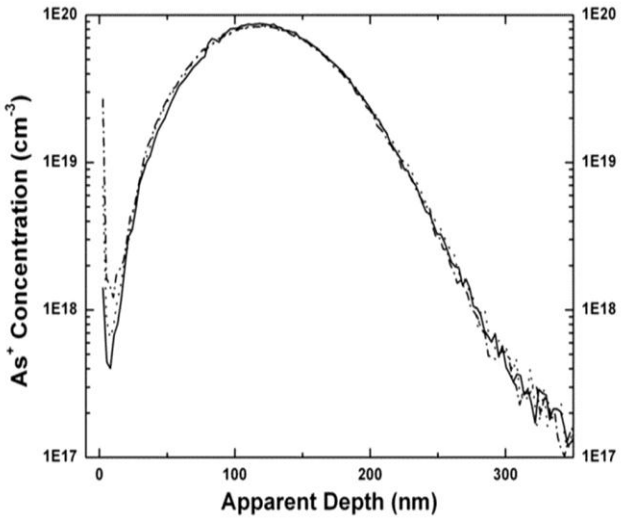

Fig. 2-7: SIMS profiles of 180keV 1×10^{15} cm^{-2} As^{+} in Si comparing unannealed and microwave-annealed wafers

— unannealed,
····· annealed for 40 s,
-·-·· annealed for 70 s.

IV. DISCUSSION

Un-assisted microwave annealing of arsenic implanted samples has shown little change in the lattice damage or sheet resistance. Arsenic implanted silicon samples heated by microwaves alone experience a steady state temperature of under 100 ^{o}C as shown in Fig. 2-2. Such low temperatures are not sufficient to remove the induced lattice damage due to the high atomic-number (*Z*) arsenic atoms. Thus, higher temperatures are required to repair implant damage and electrically activate arsenic implanted silicon while also reducing the process times.

The fundamentals of interaction of microwaves with matter can be understood through dielectric loss mechanisms. The interaction of microwaves with matter takes place through the electric field vector *E* and the magnetic field vector *H* belonging to the microwave. When subjected to an electric field, materials polarize creating an electric polarization *P*. When materials couple poorly with microwaves, a large part of the incident energy is converted to heat. There are three basic types of polarization in solids which lead to losses. The losses from space charges, arising from localized electronic conduction occur in the very low frequency region. In heavily doped Si, dipole polarization dominates at around 10^{10} Hz and is the fundamental mode of energy transfer in the microwave heating

of semiconductors [2-16]. Atomic polarization is responsible for losses in the far infrared region, for frequencies up to 10^{13} Hz; while the electrons vibrating around the nucleus give rise to electronic polarization losses[17] for frequencies in the UV region at 10^{15} Hz.

The electric field of the microwave is given by $E = E_0 e^{i\omega t}$ where E_0 is the amplitude of the field, ω is the angular frequency, t the time, and $i^2 = -1$. The resulting flux density is $D = D_0 e^{i(\omega t - \delta)}$ where δ is the phase angle associated with the time lag in polarizing the material. The electric flux density (electric displacement) comes from the applied electric field and the electric polarization: $D = \varepsilon_0 E + P = \varepsilon P$ where ε_0 is the permittivity of free space. The dielectric constant is then given by $\varepsilon_r^* = \varepsilon/\varepsilon_0 = \varepsilon_r' - i\,\varepsilon_r''$. The real part, which indicates the extent of penetration of microwaves into the material, is in phase with the field

$$\varepsilon_r^{'} = \frac{D_0}{\varepsilon_0 E \cos\delta} \tag{2-1}$$

and the imaginary part, which represents the ability of the material to absorb the microwave energy, is out of phase with the electric field E:

$$\varepsilon_r^{''} = \frac{D_0}{\varepsilon_0 E \sin\delta} \tag{2-2}$$

The loss tangent [2-17] is given by $\tan\delta = \varepsilon_r''/\varepsilon_r'$. Qualitatively, the loss tangent is the ratio of the extent of penetration of the microwave radiation, to the extent to

which the material can absorb and store that energy. The polarization losses together with conduction losses contribute to the overall dielectric loss factor ε_r''.

A material can be characterized in three ways depending on its interaction with the microwaves: transparent (low dielectric loss materials) – where microwaves pass through with little attenuation; opaque (conductors) – where microwaves are reflected and do not penetrate; and absorbing (high dielectric loss materials) – where microwaves are absorbed to a certain degree based on the value of the dielectric loss factor. The power P_{Abs} absorbed per unit volume is given by [2-18]:

$$P_{Abs} = \frac{1}{2} E_0^2 \omega \varepsilon_0 \varepsilon_r'' = \frac{1}{2} E_0^2 \omega \varepsilon_0 \varepsilon_r' \tan\delta \qquad (2\text{-}3)$$

Skin depth D_p is defined as the depth at which the electric field drops to 1/e = 0.368 of the surface value. It is given by:

$$D_p = \frac{1}{\sqrt{\pi f \mu \sigma}} \qquad (2\text{-}4)$$

where f is the frequency of the microwaves, μ is the permeability of the material and σ is the conductivity.

The polarization loss mechanism for electrical conductors differs from that of dielectrics since the free electrons in conductors propagate through the material in

the presence of an applied electric field. In this case, the conductor loses energy by resistive dissipation due to collisions of electrons with other electrons and atoms in the lattice structure. The power absorbed per unit volume in the conductor is $P = \sigma E^2$ where σ is the conductivity of the material and E is the amplitude of the electric field. For semiconductors the dissipation mechanism depends on both the frequency and conductivity of the material. For low electrical conductivity and low temperatures, dipole losses dominate. For moderate and metallic conductivity (high temperature or doped material with electrically activated dopants), Ohmic conduction losses dominate [2-19].

At microwave frequencies, the skin depth in metals is of the order of microns due to their high conductivities. Insulators like alumina, on the other hand, have a much larger skin depth allowing the microwaves to penetrate deeper without getting absorbed. Therefore microwaves are able to heat the composite susceptors more evenly than metals. Moreover, unlike metals, the resistance of semiconductors rapidly decreases with temperature which promotes rapid heating [2-17].

In the present study, susceptors made of silicon carbide dispersed in alumina are used to assist the microwave heating of implanted silicon. Thus, they are composite materials where one of the phases (SiC) is a high-loss material while

the other (alumina) is a low-loss material. Such mixed absorbers take advantage of selective heating – one of the significant characteristics of microwave heating. The microwaves are absorbed by the component that has high dielectric loss while passing through the low-loss material with little drop in energy [2-20].

The susceptor-assisted microwave heating of the implanted silicon can be understood via the polarization mechanisms described above. As the microwave annealing begins, the high-loss silicon carbide couples with the microwaves and its temperature increases. At lower anneal temperatures, the arsenic dopants in silicon are still not electrically activated and do not contribute to electronic polarization losses. As mentioned earlier, the dipole polarization losses dominate at this low conductivity and low temperatures in the initial stages of annealing.

As the temperature of the silicon carbide susceptor increases, heat is transferred from the susceptor to the silicon wafer through conduction. At any given instant, the rate P_{Cond} of heat transfer from the susceptor at temperature T_{Sus} to the silicon wafer of thickness d, cross-sectional area A and thermal conductivity σ_{th} is given by:

$$P_{cond} = A\sigma_{th}\left(\frac{T_{Sus} - T_{Si}}{d}\right) \tag{2-5}$$

As the temperature of the silicon wafer rises, the thermal energy available promotes the repair of the lattice damage caused by ion implantation. As the silicon lattice regains lattice order, dopant atoms move to occupy substitutional lattice sites. The mechanism of diffusion of arsenic in silicon is predominantly through vacancies, the interstitialcy contribution being about 10% [2-21,22]. The arsenic dopants occupying silicon lattice sites form four covalent bonds with the neighboring silicon atoms and donate the remaining electron, thereby becoming electrically active. It is these donated electrons from the dopants that are now available for electrical conduction. As the number and concentration of carrier electrons in the lattice increases, the wafer becomes more conductive. The free electrons propagate through the lattice under the action of the sinusoidally varying electric field component of the microwaves and this gives rise to Ohmic conduction losses. For wafers with high conductivity, Ohmic conduction loss is the dominant mechanism of microwave heating. Figure 2-8 depicts the dominant mechanisms in such a susceptor-assisted microwave anneal: the dipole polarization losses dominate at lower temperatures, and subsequently the Ohmic conduction losses lead to volumetric absorption of microwaves in the implanted wafers. The microwave power absorbed per unit volume is given by Eq. (2-3). Moreover, the increased conductivity leads to a decrease in the skin depth D_p associated with the absorption of microwaves, according to Eq. (2-4). The skin depth values for the three wafers microwave annealed for 40 s each are listed in

Table I. The reduction in skin depth implies absorption of microwaves occurs only in the surface layers of the wafer and the rest of the incident power is reflected, similar to the behavior of metals exposed to microwave fields. Thus, the microwave power P absorbed by the wafer decreases as the temperature T_{Si} of the wafer increases.

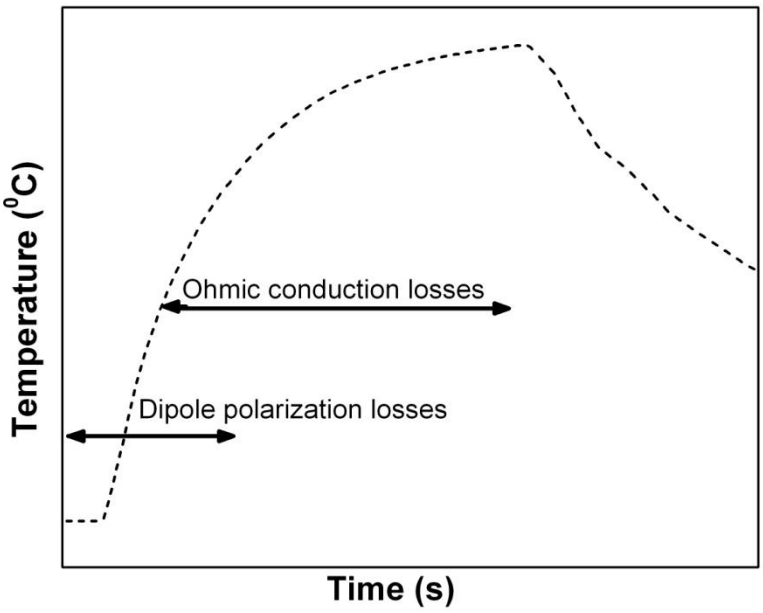

Fig. 2-8: Schematic representation of dominant mechanisms of losses in a typical susceptor-assisted microwave anneal

The peculiar shape of the temperature profile shown in Fig. 2-2 can be understood by considering the net heat exchange taking place in the system. Equation (2-5) implies that the rate of conduction of heat from the susceptor to the wafer P_{Cond} goes down as temperature T_{Si} of the wafer rises and approaches the temperature

T_{Sus} of the susceptor. Thus the silicon wafer absorbs heat both from the susceptor and the microwaves, the rates of which go down as the temperature T_{Si} of the wafer increases with time.

The wafer loses thermal energy by radiation, due to its high surface temperature. The rate of loss of heat through radiation per volume (P_{Rad}) depends on the emissivity *e*, area *A*, volume V and temperature T_{Si} of the wafer, given by the Stephan-Boltzmann Law:

$$P_{Rad} = \frac{Ae\left(T_{Si}^4 - T_{Surr}^4\right)}{V} \tag{2-6}$$

where T_{Surr} is the temperature of the surroundings to which the wafer radiates heat. The loss of thermal energy due to convection is neglected, as supported by the findings of Zohm, *et al.* [2-23], where the variations in gas density in the microwave anneal chamber was found to have no significant effect on the temperature profile.

The net power absorbed per unit volume, P_{Net}, can be related to the increase in temperature ΔT of the sample of density ρ and specific heat c_p in time *t* as:

$$P_{Net} = \rho c_p \left(\frac{\Delta T}{t}\right) \tag{2-7}$$

P_{Cond}, P_{Abs} and P_{Rad} together contribute to the net power absorbed per unit volume, P_{Net}:

$$P_{nNet} = P_{Cond} + P_{Abs} - P_{Rad} = \rho\, c_p\, (\Delta T / t) \qquad (2\text{-}8)$$

As detailed earlier, each of P_{Cond} and P_{Abs} decrease as the temperature of the wafer increases. On the other hand the rate of heat loss, P_{Rad}, increases rapidly non-linearly (as a function of T_{Si}^4). Therefore as T_{Si} increases, P_{net} decreases causing the heating rate ($\Delta T/\Delta t$) to decrease. This is in agreement with the typical observed temperature profile with a characteristic plateau as depicted in Fig. 2-2.

The minimum microwave anneal time of 40 s was determined in the following way. Initially, an attempt was made to measure the sheet resistance values of unannealed wafers, all of which were out of range for the instrument. Then, increasing annealing times of 20, 25, 30, and 35 s, were used for different samples. This was continued until a measurable value of sheet resistance was obtained on the four-point-probe station, indicating a minimum anneal time of 40 s. After this, two more anneal times of 70 s and 100 s were employed. As can be seen from Fig. 5, the sheet resistance R_s rapidly decreases with microwave annealing at 40 s and shows little decrease thereafter. This kind of behavior indicates the thermodynamic nature of the process of dopant activation. At 40 s,

typical surface temperatures achieved are about 600 ºC. Once above such temperatures, the additional annealing time improves the electrical properties of the implanted wafers only marginally, as seen from Fig. 2-5.

The fraction of arsenic dopants occupying silicon sites can be calculated using the RBS spectra. Arsenic is believed to diffuse primarily through a vacancy mechanism, making it a predominantly substitutional impurity rather than an interstitial one [2-24]. For small concentrations of impurities (<1%), the presence of impurities does not affect the channeling properties of the host lattice. Therefore the close-encounter probability of a substitutional impurity follows the same angular dependence as that of the host lattice. A first order estimate of the substitutional fraction *S* of As in Si is given by [2-25]:

$$S = \frac{(1 - \chi_{As})}{(1 - \chi_{Si})} \qquad (2\text{-}9),$$

where χ_{As} and χ_{Si} are the normalized yield comparison values for arsenic and silicon respectively. Figure 2-4 shows the values of S plotted against the anneal time. The fraction of arsenic dopants occupying silicon sites being as high as 95% indicates near-complete electrical activation.

As shown in Figs. 2-4 and 2-5, the values of S and R_{sh}, respectively saturate after 70 s of microwave anneal, which corresponds to surface temperatures of about 680 ºC. Additional microwave annealing of the samples beyond this time does not result in any significant improvement in the repair of the lattice damage or the conductivity of the implanted silicon.

The advantages of subsequent volumetric heating of implanted silicon with microwaves are two-fold: quicker processing as well as minimal diffusion of dopants during annealing. Figure 2-7 shows SIMS profiles of the arsenic dopants for different annealing times. As can be seen from the figure, the dopants do not diffuse any deeper into the silicon substrate after annealing, as compared to the profile for the unannealed sample. The electrical activation of dopants without any significant diffusion into the substrate is of crucial importance. In silicon metal-oxide-semiconductor field-effect transistors, the polysilicon gate should be diffused with a uniform heavy concentration of dopant without penetration of the dopant into the channel region through the thin gate oxide [2-26]. Conventional annealing lacks the uniform volumetric heating characteristic of microwave processing, resulting in diffusion of dopants into the channel region making the channels shorter and creating a possibility of punch-through. In this light, microwave processing comes out as a viable alternative with shortened process times and enhanced quality of dopant activation.

Figure 2-6 shows the comparison between XTEM micrographs of unannealed and microwave-annealed implanted silicon wafers. As indicated in Fig. 2-6a, the amorphous layer present at the surface in the unannealed samples can be distinguished as the lightly shaded area. Fig. 2-6b displays the XTEM micrograph of the same sample after microwave annealing for 40 s. It is seen that the amorphous silicon layer has crystallized, but with a small band of defects present at about 50 nm from the surface which is about twice the projected range for arsenic dopants at 30 keV. Ion irradiation can give rise to deep-level interstitials which can then coagulate to form the defect band as seen in Fig. 2-6b. Employing the +1 model of implant-induced damage indicates an excess of interstitials after vacancy-interstitial annihilation during annealing of the damaged silicon [2-27, 28]. The excess interstitials lie at the end of range (EOR) of the implant, at a depth approximately equal to the thickness of the amorphous layer in unannealed samples. RUMP modeling of spectra corresponding to the as-implanted samples gives the approximate thickness of the amorphous layer to be 50 nm, which is roughly twice the projected range of the 30 keV arsenic implantation species. There are no dislocation networks indicative of nucleated crystal growth within the amorphous layer. This indicates that the crystal regrowth mechanism during microwave annealing is SPEG, nucleating at twice the projected range ($2R_p$) [2-3, 6]. This agrees with the XTEM micrographs observed by Alford *et al.* [2-13].

V. CONCLUSION

This work has demonstrated that susceptor-assisted microwave processing is a viable means of dopant activation and damage repair in ion-implanted silicon. Arsenic implanted silicon samples were microwave processed assisted by SiC susceptors, to temperatures required for solid phase epitaxy in silicon. The susceptor-assisted heating allowed attainment of temperatures above 700 ºC and thereby reducing processing times as well as achieving near-complete electrical activation of the dopants. Different microwave loss mechanisms were responsible for the conversion of microwave power to heat in the experimental set-up: dipole polarization losses in the susceptor in the low-temperature range and Ohmic conduction losses in the ion-implanted silicon in the high-temperature range. Sample surface temperatures ranged 620-730 ^{o}C. The characteristic shape of the temperature profile was explained. Microwave processing of arsenic-implanted silicon, for 40-100 s, resulted in the repair of nearly all radiation damage as monitored by sheet resistance and RBS. The process of dopant activation was observed to not be kinetically limited above a surface temperature of 680 ºC. Moreover, electrical activation of the dopants was achieved without any significant diffusion of the dopants deeper into the substrate, which is advantageous for the processing of modern field-effect transistors.

Chapter 3

EFFECT OF ANNEALING IN DIFFERENT ENVIRONMENTS ON ELECTRICAL AND OPTICAL PROPERTIES OF a-IZO FILMS ON POLYETHYLENE NAPHTHALATE

I. INTRODUCTION

Recent years have seen a tremendous increase in research activity in the area of flexible display technologies. Once developed, flexible flat panel display technologies will offer advantages like very thin profiles, lightweight and robust display systems, extreme portability due to the ability to flex, curve, conform, roll and fold a display, high throughput manufacturing, wearable displays integrated in garments and engineering design freedom. Two of the most important enabling technologies for flexible displays are transparent conducting layers and flexible substrates [3-1 - 3-3]. The flexible substrate used in the present study – polyethylene naphthalate (PEN) – is prepared by a process where the amorphous cast is drawn both in the machine direction and the transverse direction. The biaxially oriented film is then heat-set to crystallize it [3-3]. PEN films show lower coefficient of thermal expansion (CTE = 13 ppm/^{o}C), than polyethylene terephthalate (PET) films (CTE = 15 ppm/^{o}C). PEN also has higher values of Young's modulus and tensile strength than PET, making it a substrate with better mechanical properties than PET [3-3]. The thermo-mechanical analysis carried

out by McDonald *et al.*, shows that PEN suffers no elongation after it reaches the selected temperatures in the range 150ºC-200ºC at which it is held for 2 hours [3-4].

For comparison of transparent conducting materials, Haacke [3-5] proposed a figure of merit (FOM) as $\frac{T_{avg}^{10}}{R_s}$; where T_{avg} is the average optical transmittance and R_s is the sheet resistance. Currently, amorphous indium zinc oxide (a-IZO) is a material of great interest for transparent conducting layer applications because it has better etch characteristics than crystalline indium tin oxide (c-ITO) and also offers slightly lower resistivity than amorphous ITO (a-ITO) [3-6]. Amorphous IZO is also structurally stable and can be deposited onto unheated substrates, making it appropriate for use on polymeric substrates [3-5]. Han *et al.* have reported the crystallization of ITO films on PEN by annealing in air at 150 ºC [3-7].

Polymer substrates are more advantageous than glass in terms of the flexibility and ease of handling; but their low glass-transition temperature (T_g) limit the process temperatures that can be used for subsequent display fabrication [3-3]. While PEN has a T_g of 120 ºC, its dimensional stability can be enhanced by heat stabilization, making it dimensionally reproducible up to 200 ºC. This temperature

is within the performance requirements of a flexible substrate for an OLED display [3-8]. In this paper, we report a 62-fold increase in the FOM of a-IZO films deposited on PEN upon annealing in air for 6 hrs. The effect of anneal in various environments on the electrical and optical properties, along with the conduction mechanism and factors governing carrier mobility is investigated. We also report near-complete reversal of degraded electrical properties on annealing in oxygen environment by subjecting the films to vacuum anneal.

II. EXPERIMENTAL

The a-IZO films were deposited on a 125 μm thick PEN substrate. The composition of the sputtering target was 40% In_2O_3 and 60% ZnO. The deposition was done at 300 W DC power and 16 mTorr of pressure, with 2% oxygen and balance argon. The thin film samples were annealed in different environments: air, oxygen and vacuum at 150 ºC for 2, 4, and 6 hrs. Electrical, optical, and surface characterization was carried out before and after each of the anneal steps. Sheet resistance measurements were done by contacting the sample surface with an in-line four-point-probe equipped with a 100 mA Keithley 2700 digital multimeter. To determine carrier concentration and mobility, Hall-effect measurement was employed with the use of an Ecopia HMS-3000 Hall effect measurement system. To achieve an Ohmic contact with the a-IZO films, Ti/Au

contacts were deposited [3-9] employing a Denton physical vapor deposition system. The surface roughness of the a-IZO films was studied by atomic force microscopy (AFM) in acoustic mode (tapping mode), using a Molecular Imaging Pico SPM system. The optical transmittance and reflectivity of the films were measured with an Ocean Optics double channel spectrometer (model DS200) in the wavelength range of 300-800 nm. To study the extent of reversibility of degradation in the electrical properties upon annealing the films in oxygen, the films were subjected to vacuum anneals and their electrical and optical properties were measured after the anneals.

III. RESULTS

Figure 3-1 shows the dependence of sheet resistance on annealing time in various annealing environments. For comparison, the sheet resistance of as-deposited films is also shown. A 6 hr air-anneal results in a 45-fold decrease in sheet resistance, while the vacuum anneal results in a 12-fold reduction. In case of the oxygen ambient, the sheet resistance increased with increasing anneal times after an initial decrease, reaching 10^6 Ω/sq after 6 hours of anneal. Figure 3-2 shows the variation in carrier concentration and carrier mobility in the a-IZO films which were annealed in air and vacuum. As the anneal time progresses, an increase in

carrier concentration is observed in both cases with vacuum-anneals resulting in higher carrier concentrations than the air-anneals. While the air-annealed samples show improved mobility, films annealed in vacuum show a decrease as anneal time increases. The films annealed in oxygen did not show reproducible carrier concentration and mobility values due to the increased resistivity.

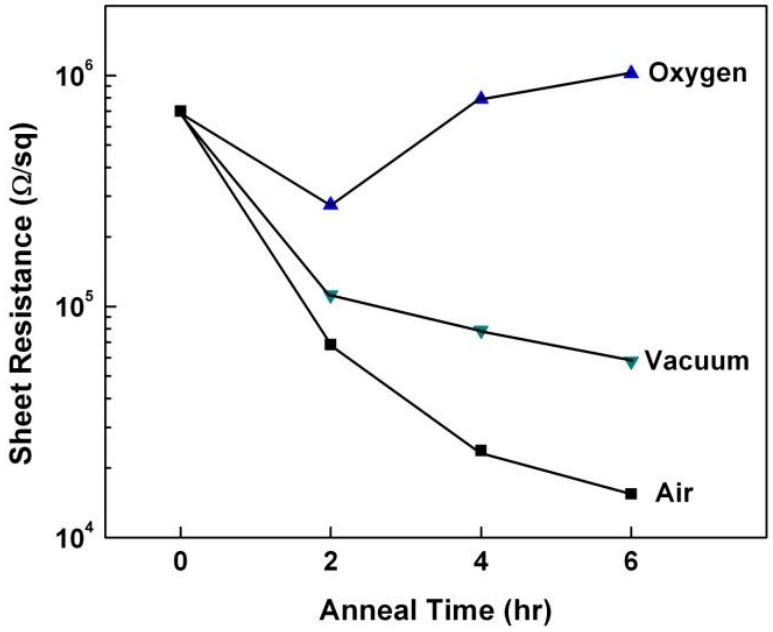

Fig. 3-1: Sheet resistance of as-deposited and annealed a-IZO films on PEN. Annealing temperature was 150 ºC.

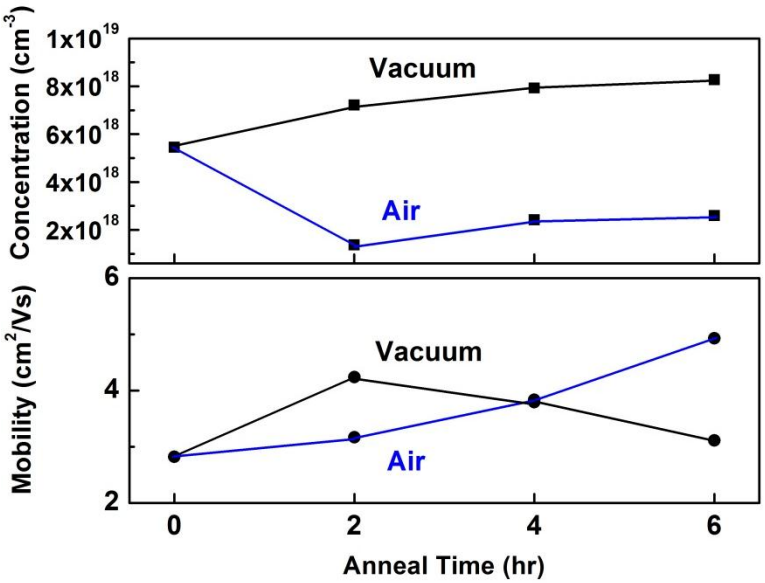

Fig. 3-2: Carrier concentration and carrier mobility as functions of anneal time, for a-IZO films on PEN annealed in air and vacuum

Figure 3-3 displays the transmittance spectra for un-annealed a-IZO films and those annealed for 6 hrs in the different anneal environments. To determine the Haacke figure of merit, the value of T_{avg} was calculated as [3-10]:

$$T_{avg} = \frac{\int V(\lambda)T(\lambda)d\lambda}{\int V(\lambda)d\lambda} \tag{3-1}$$

where $T(\lambda)$ is the transmittance and $V(\lambda)$ is the photopic luminous efficiency function defining the standard observer for photometry. After 6 hours of annealing in air, vacuum and oxygen, the values for the FOM were 9.0×10^{-6}, 2.4×10^{-6}, and $1.2\times10^{-7}\Omega^{-1}$, respectively; while un-annealed films gave a value of $1.4\times10^{-7}\ \Omega^{-1}$; giving a 62-fold improvement upon annealing in air.

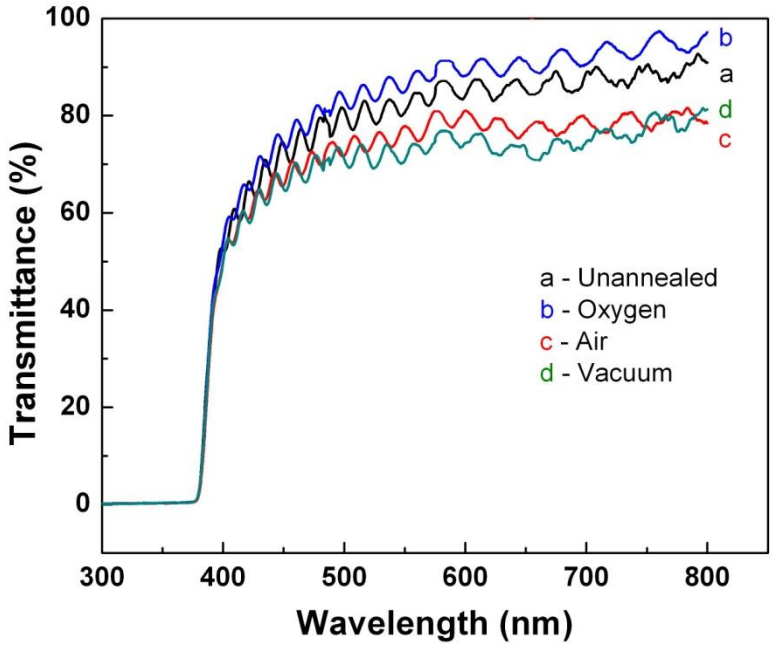

Fig. 3-3: UV-Vis Transmittance spectra of un-annealed and annealed a-IZO films on PEN

As seen in Fig. 3-3, the optical transmittance of as-deposited a-IZO films is above 80% for most of the visible range of wavelengths. Figure 3-4 depicts the atomic force micrograph of a-IZO films annealed in air. The RMS surface roughness is seen to be 2.04 nm. Similar values were obtained for as-deposited, vacuum-annealed and oxygen-annealed films (not shown), indicating no significant effect of annealing environments on the surface roughness.

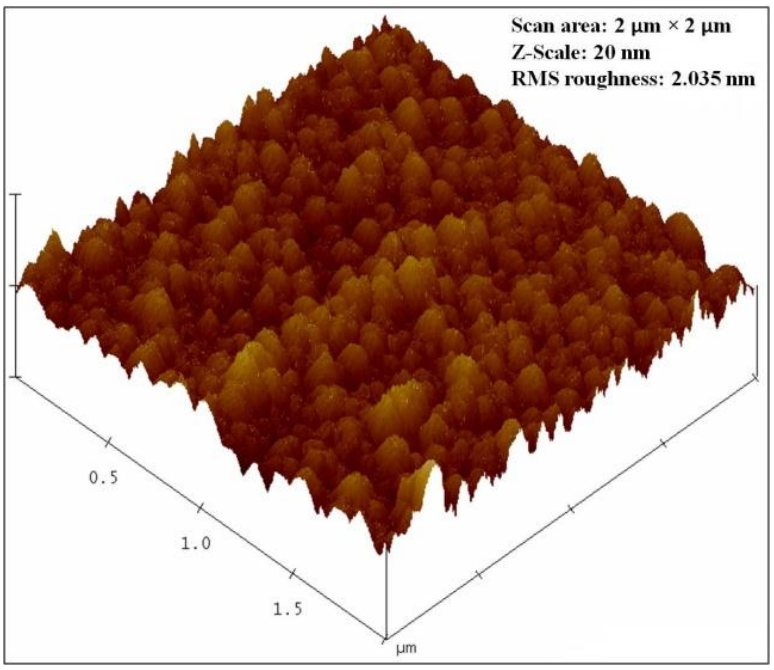

Fig. 3-4: Atomic force micrograph of a-IZO films deposited on PEN and annealed for 6 hr at 150 ºC in air

Figure 3-5 shows the variation of carrier concentration and carrier mobility with increasing anneal time for oxygen-annealed films subsequently annealed in vacuum, as compared to those annealed in vacuum. It is seen that with a 6 hr anneal in vacuum the films nearly regain the carrier concentration and mobility. This demonstrates the reversibility of degradation in electrical properties after oxygen-anneals. Hence, vacuum-anneals offer a way of reversing the effects of oxidizing environments on a-IZO thin films. Figure 3-6 shows the transmittance spectra for films annealed in vacuum and films annealed first in oxygen followed

by a vacuum-anneal. For comparison, the transmittance spectrum of unannealed a-IZO films is also shown.

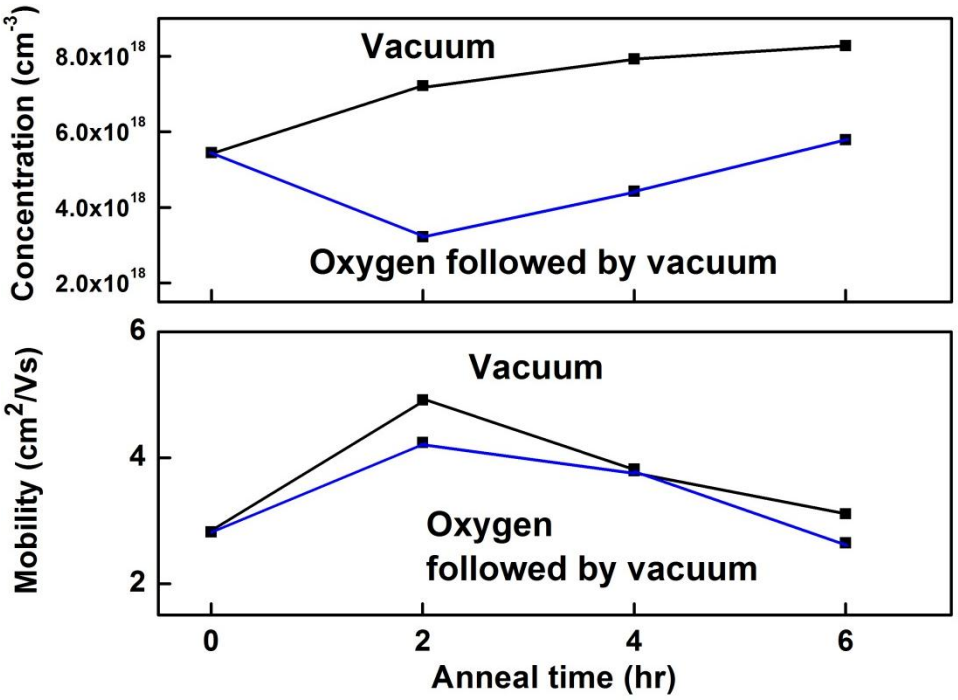

Fig. 3-5: Carrier concentration and carrier mobility as functions of anneal time, for a-IZO films on PEN annealed in vacuum; and a-IZO films annealed in oxygen followed by annealing in vacuum

Figure 3-7 shows the change in the absorption coefficient with incident energy on a-IZO films on PEN, annealed in different environments. The band-gap E_g is determined using $\alpha(h\,\nu) \propto (h\,\nu - E_g)^{1/2}$. The effective combined band-gap of the a-IZO+PEN structure is seen to be around 3.15 eV. From Fig. 3-7 it is seen that as the carrier concentration increases for the films after the anneals in air and vacuum. It is also noted that the effective band-gap undergoes a blueshift, according to the Burnstein-Moss effect [3-11].

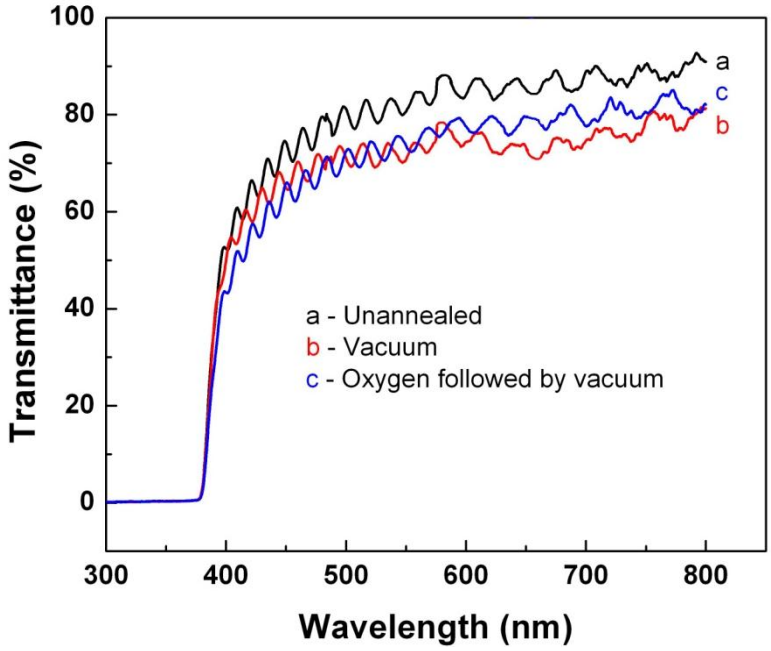

Fig. 3-6: UV-Vis Transmittance spectra for a-IZO films on PEN annealed in vacuum; and in oxygen followed by annealing in vacuum

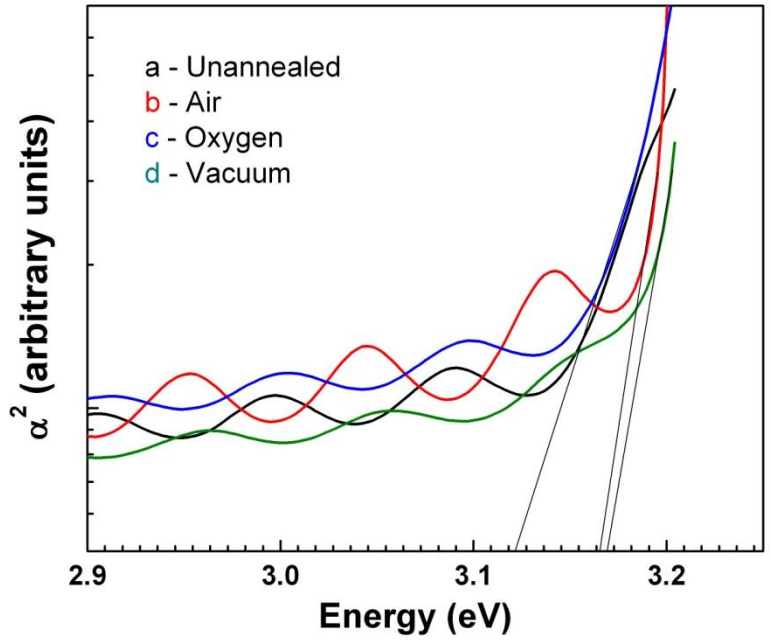

Figure 3-7: Determination of the effective optical band gap for a-IZO films annealed in different environments

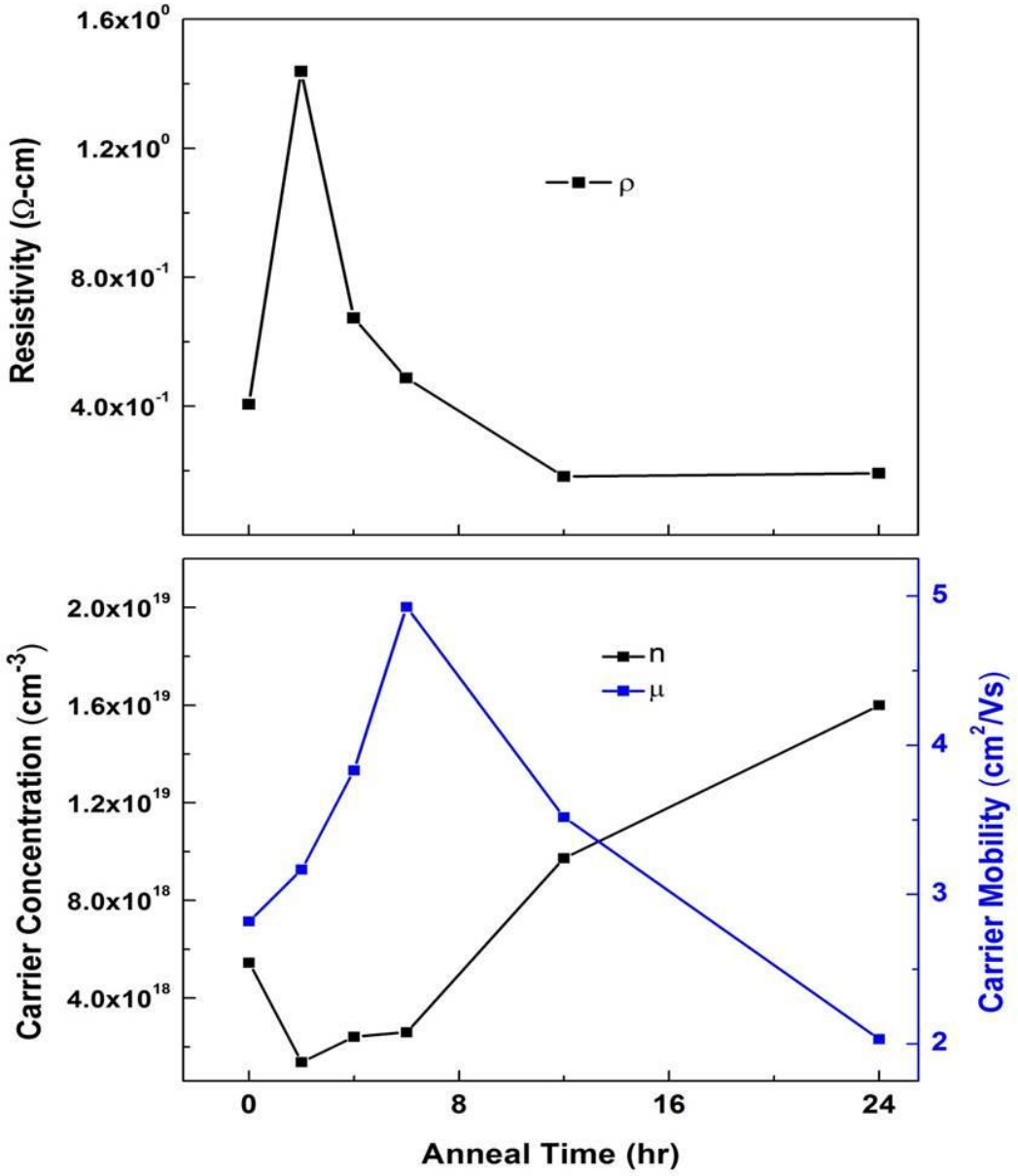

Figure 3-8: Resistivity, carrier concentration and carrier mobility as functions of anneal time, for a-IZO films on PEN annealed in air at 150 °C

The a-IZO thin films on PEN were also subjected to longer anneals in air at 150 °C for 12 and 24 hours, to investigate their stability. The effect of the anneals on

their electrical properties was also studied. Figure 3-8 shows the variation in resistivity, carrier concentration and carrier mobility for the a-IZO films annealed in air at 150 °C for 0, 2, 4, 6, 12 and 24 hrs. After an initial decrease in the carrier concentration with a corresponding increase in the carrier mobility, the carrier concentration is seen to rise with increasing anneal time. The carrier mobility suffers a significant reduction. Initially, the resistivity increases significantly but then slowly decreases with longer anneals.

IV. DISCUSSION

While efforts to control properties of IZO films on PET by changing the amount of hydrogen and oxygen gas as well as sputtering parameters during deposition have been reported [3-12 – 3-15]; studying the effect of anneal environments is useful in understanding the conduction mechanisms as well as improving performance of the films post-deposition. Electronic conduction in oxide semiconductors such as a-IZO depends on the number of vacancies as the source of free carriers and is independent of structural disorder [3-16]. This is reflected in the difference in electrical properties upon annealing in environments with varying concentrations of oxygen. At low oxygen concentrations, doubly charged oxygen vacancies are created: $O_o^x = \frac{1}{2} O_{2(g)} + V_o^{\cdot\cdot} + 2 e^-$. At high oxygen partial pressure, doubly charged oxygen vacancies are consumed as the reaction above is

reversed, decreasing the carrier concentration. Free carriers are created at low oxygen potentials, as the reaction proceeds to the right [3-6]. This is reflected in the increased carrier concentration as shown in Fig. 3-1 and Fig. 3-2.

As seen in Fig. 3-3, the transmittance spectra of films annealed in different environments differ significantly in the red wavelength region. In this region, the transmittance is mainly influenced by free carrier absorption where a high concentration of carriers results in more absorption and lower transmittance [3-16]. For films annealed in oxygen, the transmittance is higher at longer wavelengths due to the lower concentration of carriers. For air-annealed and vacuum-annealed films, higher carrier concentration results in lower transmittance as compared to unannealed and oxygen-annealed films. FOM calculations using the data in Fig. 3-1 and Fig. 3-3 reveal that annealing in air gives the best FOM; indicating that for an optimum intermediate concentration of oxygen in the annealing environment, a significant increase in both electrical and optical properties can be achieved.

As shown in Fig. 3-8, the long air-anneals at 150 °C do not seem to degrade the a-IZO films deposited on PEN. There is a significant reduction in the resistivity obtained as the anneal time increases. The carrier mobility shows a reduction corresponding to the increase in carrier concentration, indicating that the

dominant mechanism of carrier scattering is through ionized impurities at those high levels of carrier concentration.

Figure 3-9 depicts the relation between carrier concentration and carrier mobility for a-IZO films annealed in air. Carrier mobility calculated using a model based on electron scattering due to changes in texture and grain structure of the film [3-18, 19] is also shown. The mobility was calculated as:

$$\mu = \sqrt{2\pi}\,\frac{(\varepsilon_r\varepsilon_0)^2 d^2 (kT)^{3/2}}{N_d e^3 f^2 \lambda_d \sqrt{m}} \tag{3-3}$$

where $\lambda_d = \left(\frac{\varepsilon_r\varepsilon_0 k_B T}{e^2 N}\right)^{1/2}$ is the Debye screening length. The dielectric constant (ε_r) of IZO is 8.1, estimated distance between acceptor centers (d) is 0.6 nm, density of acceptor-like surface defects (N_d) is 4×10^{14}cm^{-2}, occupancy fraction of acceptor centers (f) is 0.9, N is the carrier concentration, ε_0 is the permittivity of free space, T is temperature and k_B is the Boltzmann constant [3-18]. The close agreement between the measured and calculated carrier mobility values at low carrier concentrations (1-4×10^{18} cm^{-3}) indicates that the mobility is mainly limited by texture and structural defects.

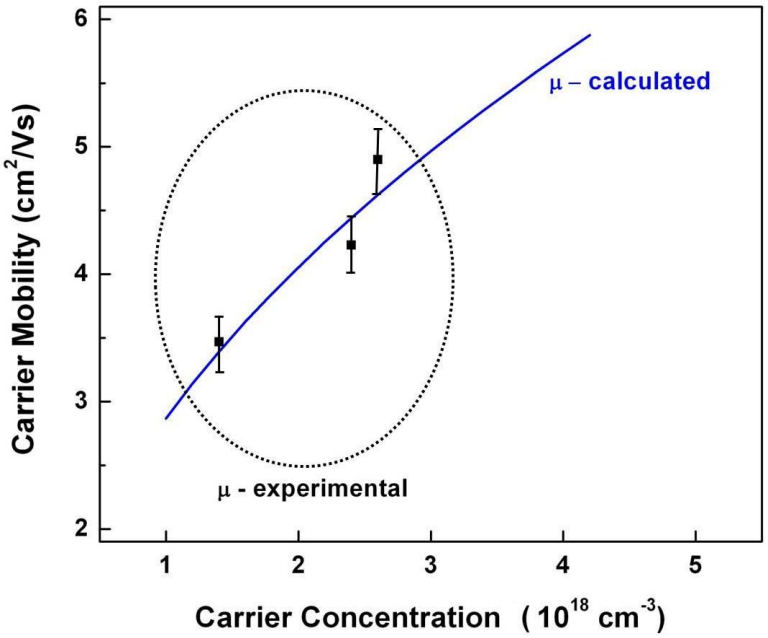

Figure 3-9: Mobility as a function of carrier concentration of a-IZO films on PEN: comparison between the calculated and measured mobility values for films annealed in air

V. CONCLUSIONS

In conclusion, the impact of low-temperature anneals in air, oxygen and vacuum, on the properties of a-IZO thin films grown on a PEN was investigated. An approximately 62-fold increase in the Haacke FOM was achieved by annealing the films in air at 150 ºC for 6 hrs. Difference in electrical performance of films annealed in different environments resulted from change in the concentration of oxygen vacancies. It was demonstrated that the degradation in the electrical properties upon exposure to oxidizing environment can be reversed by employing

further vacuum anneals. The agreement between the measured values of carrier mobility and the values calculated using a model showed that the mobility was influenced by structural defects at low carrier concentrations.

Chapter 4

HIGHEST TRANSMITTANCE AND HIGH-MOBILITY AMORPHOUS INDIUM GALLIUM ZINC OXIDE FILMS ON FLEXIBLE SUBSTRATE BY ROOM-TEMPERATURE DEPOSITION AND POST-DEPOSITION ANNEALS

I. INTRODUCTION

Transparent conducting oxides (TCOs) are characterized by high electrical conductivity approaching that of metals, and high transmittance (>80%) in the visible region of the electromagnetic spectrum. Single-component TCOs such as zinc oxide [4-1 – 4-3] and tin oxide [4-4] have been studied extensively. For the past two decades, there has been increasing interest in multi-component TCOs with multiple cation oxides such as indium tin oxide [4-5], indium zinc oxide [4-6], zinc tin oxide [4-7] *etc*. Among them, amorphous indium gallium zinc oxide (a-IGZO) has emerged as a promising candidate since the report of high-mobility (~10 cm^2/Vs) films by Nomura *et al.* [4-8]. Such high-mobility amorphous TCOs find applications as channel layer materials in thin film transistors in flexible electronics [4-9,10]. The bottom of the conduction band in amorphous oxide semiconductors with post-transition-metal cations is essentially made of isotropic, spatially spread metal *ns* orbitals (where *n* is the principal quantum number). There is a direct overlap between neighboring metal *ns* orbitals which is not

affected by distorted chemical bonds which are present in the amorphous state. Thus the amorphous oxide semiconductors, which can be formed at room temperature, show mobilities similar to those of the corresponding crystalline phases [4-8, 4-11]. Hosono *et. al.* have illustrated the various advantages of amorphous oxides. [4-12, 4-13]. The manufacturability at room-temperature makes amorphous materials very attractive. Moreover, at such low temperatures, the oxides show smooth surfaces, which is advantageous for process integration. The disadvantages of having grain boundaries are also avoided. Hosono *et. al.* argue that the electronic transport in amorphous oxides is fundamentally different from that in silicon or a similar covalent semiconductor because the covalent conductors show strongly-directed sp^3 bonds. Unlike these, the amorphous oxide semiconductors with post-transition metal cations where the isotropic and spatially expanded 4s, 5s and 6s orbitals form the conduction band minima. The oxide nature of these semiconductors implies air-processibility and thermodynamic stability. Amorphous IGZO is thermally stable in air up to ~500 °C [4-8].

Several aspects of amorphous indium gallium zinc oxide (a-IGZO) make it an attractive choice among the amorphous semiconductors. The Hall mobility of both crystalline and amorphous IGZO increases with increasing carrier concentration. In traditional covalent semiconductors, higher doping

concentration leads to increased ionized impurity scattering resulting in lower mobility. In IGZO the trend could be explained as follows [4-8]: in crystalline IGZO, as the doping concentration increases, the Fermi level rises, lowering the potential barrier experienced by the conduction band electrons due to grain boundaries, which are modeled as back-to-back Schottky barriers [4-14]. In a similar fashion, Nomura *et. al.* [4-8] explain the trend in a-IGZO in attributing it to the percolation model in which the tail state potential barriers resulting from the random amorphous bonding structure. Another property of IGZO as a choice for transparent thin film transistor (TTFT) channel material is the tenability of carrier concentration up to as low as 10^{14} cm^{-3} in order to achieve a low off current and a large drain on-to-off ratio [4-8].

Amorphous IGZO films have been deposited employing various processes such as RF co-sputtering onto glass [4-15], and pulsed laser deposition (PLD) onto glass [4-16] and sputter deposition onto polyethylene terephthalate (PET) [4-8]. Low resistivity (7×10^{-4} Ω-cm) and high carrier mobility (16.6 cm^2/V-s) a-IGZO films have been reported in the past, relegated to processing at elevated substrate temperatures [4-15,4-16]. High processing temperatures are not suitable for polymer-based substrates used in flexible optoelectronics [4-17]. Suresh *et al.* have reported degraded conductivity of a-IGZO films upon annealing in air [4-18]. In the present chapter, room-temperature RF sputter deposition of a-IGZO

films onto flexible polymer substrates of polyethylene naphthalate (PEN) is reported. This part of the study achieved the highest transmittance (93%) reported in the literature along with high carrier mobility (17 cm^2/V-s). The films were annealed in different environments to further enhance the electrical and optical properties. Carrier mobilities were calculated using a model based on film texture and structural defects which showed a close agreement with the experimentally measured values.

II. EXPERIMENTAL

The a-IGZO films were deposited on PEN (Dupont Teonex® Q65) at room temperature using an RF sputter deposition system. The composition of the sputtering target was 99.99% $InGaZnO_4$.The deposition was done at 100 W RF power and 10 mTorr of pressure using argon gas. Rutherford backscattering spectrometry (RBS) with a 2 MeV He^{++} ion beam was used to determine the composition of the thin films. Variable angle spectroscopic ellipsometry (VASE) analysis was done to determine the film thickness. Surface roughness was elucidated by atomic force microscopy (AFM) in acoustic mode (tapping mode), using a Molecular Imaging Pico SPM system. The thin film samples were annealed in different environments: air, oxygen, and vacuum at 150 ºC for 2, 4, and 6 hrs. Electrical and optical characterization was done before, and after each

of the anneal steps. Sheet resistance was measured by contacting the sample surface with an in-line four-point-probe equipped with a 100 mA Keithley 2700 digital multimeter. To determine carrier concentration and mobility, Hall-effect measurements were done with the use of an Ecopia HMS-3000 Hall effect measurement system. The optical transmittance and reflectivity of the films were measured with an Ocean Optics double channel spectrometer (model DS200) in the wavelength range of 300-800 nm. To study the extent of reversibility of degradation in the electrical properties upon annealing the films in oxygen, equal duration of vacuum anneals were done and the electrical and optical properties of the films were measured.

III. RESULTS

The backscattering spectrum obtained from as-deposited a-IGZO thin films along with the RUMP simulation is shown in Fig. 4-1. The analysis revealed the film composition to be $InGaZn_{0.76}O_3$ demonstrating the oxygen-deficient nature of the films. The relative proportion of Ga and Zn was obtained using Helium-Induced X-Ray Emission (HeXE) analysis employing the same tandetron accelerator used for RBS. Film thickness was determined to be approximately 85 nm using VASE. The surface roughness of as-deposited films was found to be about 0.8 nm.

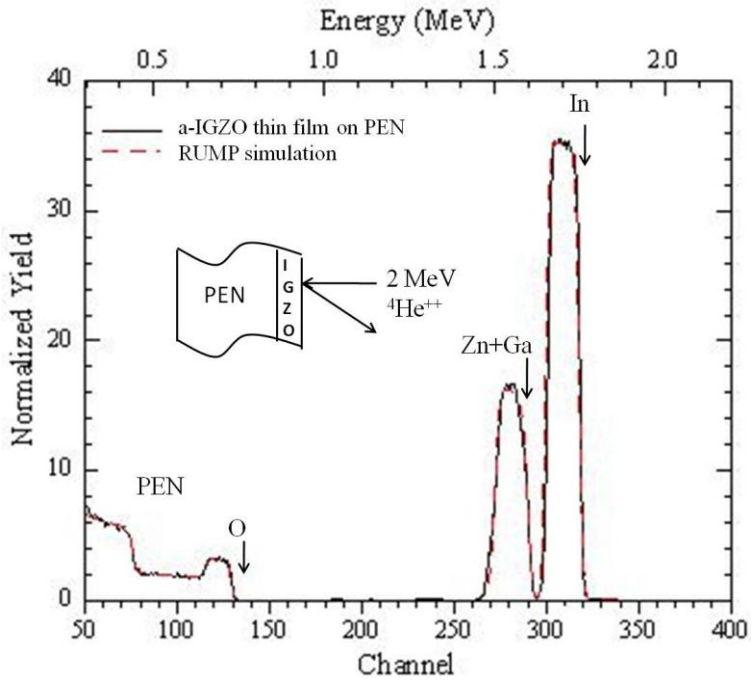

Fig. **4-1**: Backscattering spectrum along with the RUMP simulation for the as-deposited a-IGZO thin films on PEN.

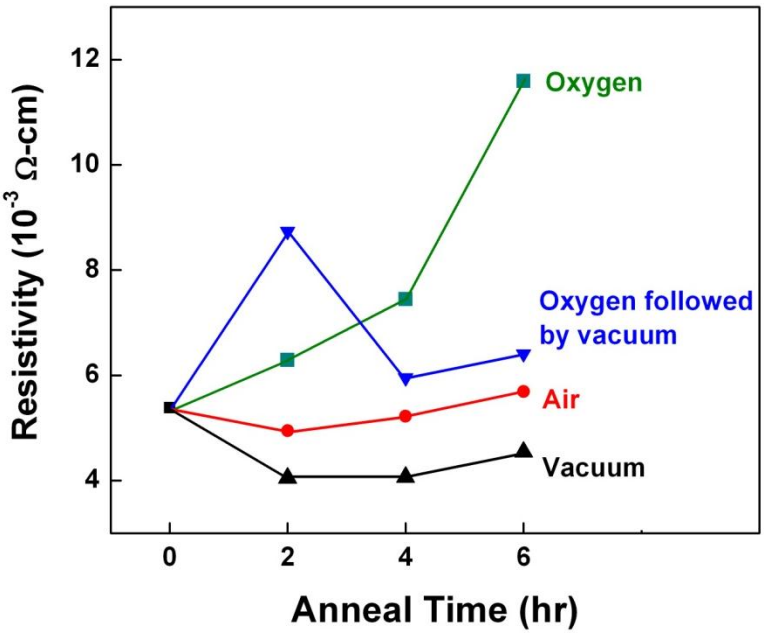

Fig. **4-2**: Variation in the resistivity of a-IGZO films annealed at 150 ºC in different environments

Figure 4-2 shows the dependence of resistivity on annealing time in various annealing environments. For comparison, the resistivity of as-deposited films is also shown. Six-hour vacuum-anneals result in a decrease in resistivity to values below 5×10^{-3} Ω-cm; while, the air and oxygen anneals display a gradually increase the resistivity. Figure 4-3 shows the variation in carrier concentration and carrier mobility in the a-IGZO films annealed in different environments. As the anneal time progresses, an increase in carrier concentration is observed for vacuum-annealed films and values of carrier concentrations reaching 10^{20} cm^{-3}. Air and oxygen-anneals result in continuous decrease in the carrier concentrations. The air-annealed samples show improved mobility; whereas, vacuum-annealed films show a decrease in mobility as anneal time increased. As shown in Figs. 4-2 and 4-3, the films subjected to oxygen-anneals followed by vacuum-anneals show a significant improvement over oxygen-annealed films and demonstrate a reversibility of the degrading effects upon annealing.

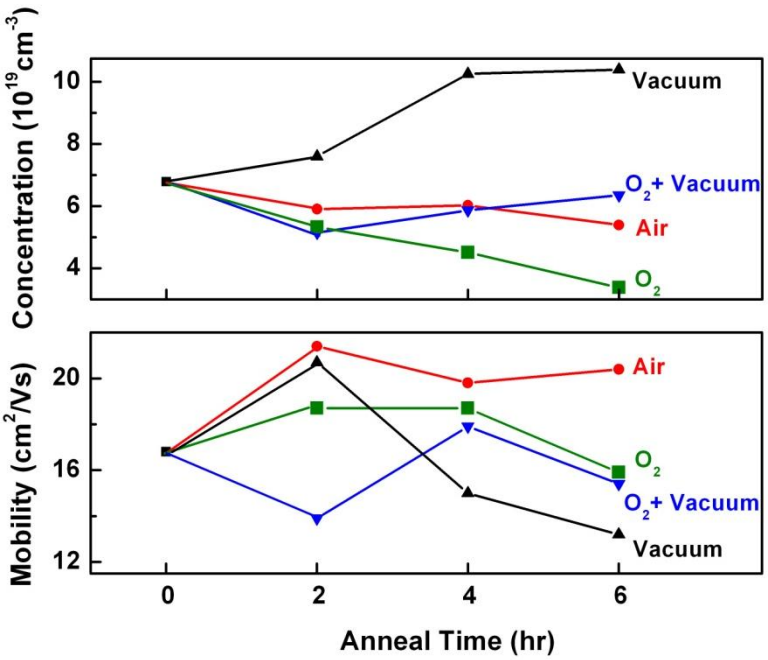

Fig. 4-3: Variation in carrier concentration and carrier mobility with increasing anneal time for a-IGZO films annealed at 150 ºC in different environments

Figure 4-4 displays the transmittance spectra for un-annealed a-IGZO films and those annealed for 6 hrs in the different anneal environments. For comparison of transparent conducting materials, Haacke [4-19] proposed a figure of merit (FOM) as $\frac{T_{avg}^{10}}{R_s}$; where T_{avg} is the average optical transmittance and R_s is the sheet resistance. To determine the Haacke figure of merit, the value of T_{avg} was calculated as [4-20]:

$$T_{avg} = \frac{\int V(\lambda)T(\lambda)d\lambda}{\int V(\lambda)d\lambda} \qquad (4\text{-}1)$$

where $T(\lambda)$ is the transmittance and $V(\lambda)$ is the photopic luminous efficiency function defining the standard observer for photometry. The T_{avg} for the as-deposited films was 93.8%, giving an FOM of 5×10^{-4}. After 6 hours of annealing in air, oxygen and vacuum, the values for the FOM were 4.4×10^{-4}, 1.3×10^{-4}, and $6.2\times10^{-7}\Omega^{-1}$, respectively; showing a 25% improvement in FOM after vacuum-anneals.

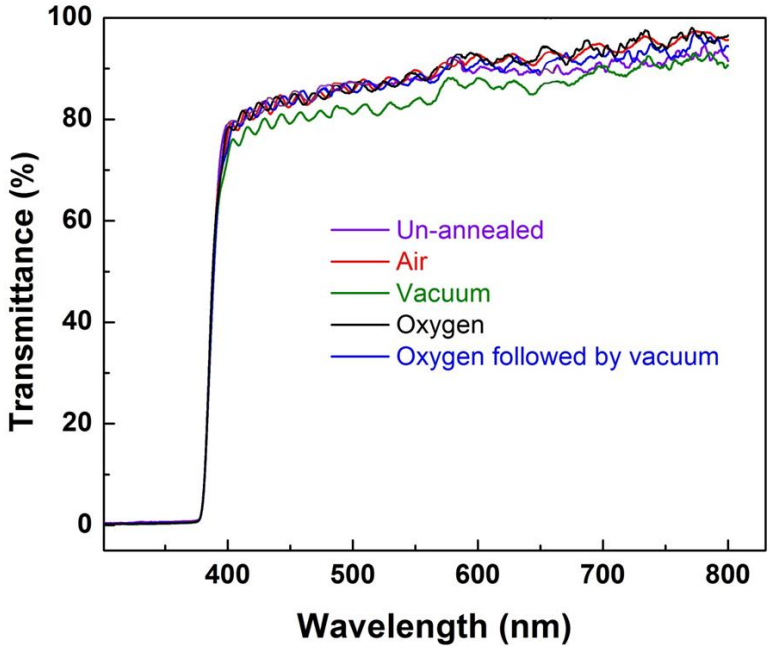

Fig. 4-4: UV-Vis transmittance spectra of un-annealed and annealed a-IGZO films on PEN substrates

As seen in Fig. 4-4, the optical transmittance of as-deposited a-IGZO films is above 85% for most of the visible range of wavelengths. The annealed films show lower transmittance for short wavelengths due to higher reflectance. The transmittance in the longer wavelength region is mainly influenced by free carrier

absorption [4-21]. For films annealed in oxygen, the transmittance is higher at longer wavelengths due to the lower concentration of carriers. For air-annealed and vacuum-annealed films, higher carrier concentration results in lower transmittance as compared to the oxygen-annealed films. The transmittance of a-IGZO films subjected to oxygen-anneals followed by vacuum-anneals shows a downward shift towards that of the films annealed in vacuum, showing the partial reversibility of the effects of oxygen anneal on the optical properties.

IV. DISCUSSION

Studying the effect of anneal environments is useful in understanding the conduction mechanisms as well as improving performance of the films post-deposition. Electronic conduction in oxide semiconductors depends on the number of vacancies as the source of free carriers and is independent of structural disorder [4-22]. This is reflected in the difference in electrical properties upon annealing in environments with varying concentrations of oxygen. At low oxygen concentrations, doubly charged oxygen vacancies are created: $O_o^x = ½\ O_{2(g)} + V^{\cdot\cdot}_o + 2\ e^-$. At high oxygen partial pressure, doubly charged oxygen vacancies are consumed as the reaction above is reversed, decreasing the carrier concentration. Free carriers are created at low oxygen potentials, as the reaction proceeds to the right [4-23]. This is reflected in the increased carrier concentration as shown in

Fig. 4-3. The oxygen vacancies act as ionic scattering centers for the electrons; this explains the decrease in carrier mobility at high carrier concentrations (> 6×10^{19} cm^{-3}).

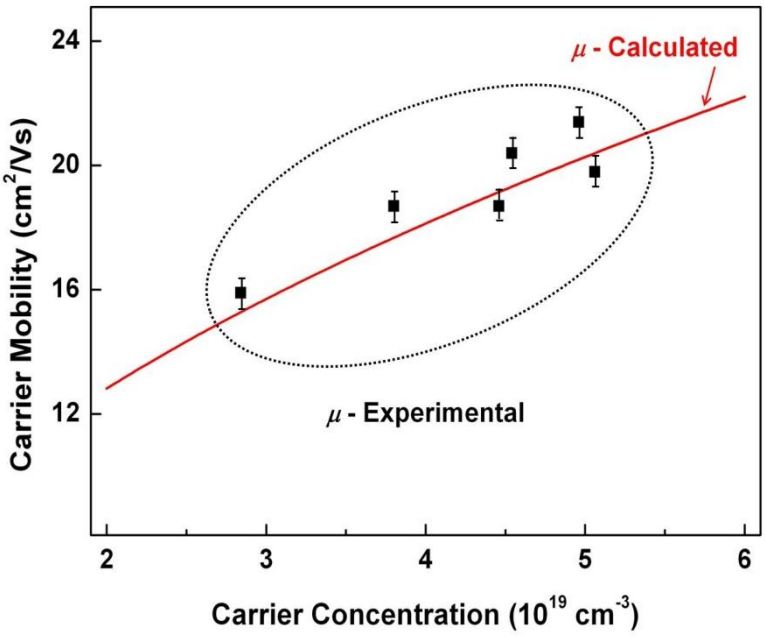

Fig. 4-5: Carrier mobility as a function of carrier concentration in a-IGZO films on PEN: a comparison between the calculated and measured mobility values

Figure 4-5 depicts the dependence of carrier mobility on the carrier concentration for a-IGZO films. For amorphous indium zinc oxide (a-IZO) films, carrier mobility calculations have been done based on a model for electron scattering due to changes in texture and grain structure of the film [4-24]. The extension of this model allows for the determination of carrier mobility in a-IGZO films as:

$$\mu = \sqrt{2\pi}\,\frac{(\varepsilon_r\varepsilon_0)^2 d^2 (kT)^{3/2}}{N_d e^3 f^2 \lambda_d \sqrt{m}} \tag{4-2}$$

where $\lambda_d = \left(\frac{\varepsilon_r \varepsilon_0 k_B T}{e^2 N}\right)^{1/2}$ is the Debye screening length. Values of dielectric constant (ε_r), the estimated distance between acceptor centers (d), density of acceptor-like surface defects (N_d), occupancy fraction of acceptor centers (f) are similar to those used for a-IZO films by Martins *et al.* [2-24]. N is the carrier concentration, ε_0 is the permittivity of free space, T is temperature and k_B is the Boltzmann constant. The close agreement between the measured and calculated carrier mobility values indicates that the mobility is mainly limited by texture and structural defects at low carrier concentrations (2-6×10^{19} cm^{-3}).

V. CONCLUSION

In summary, a-IGZO thin films of the highest transmittance reported in literature were deposited onto flexible polymer substrates at room temperature. The films were annealed in vacuum, air, and oxygen to enhance electrical and optical performance. Electrical and optical characterization was done before and after annealing. A partial reversal of the degradation in electrical properties upon annealing in oxygen was achieved by subjecting the films to subsequent vacuum anneal. A model based on film texture and structural defects which showed close agreement between the measured and calculated carrier mobility values.

Chapter 5

HIGHEST TRANSMITTANCE AND HIGH-MOBILITY A-IGZO FILMS ON FLEXIBLE SUBSTRATE BY ROOM-TEMPERATURE DEPOSITION AND POST-DEPOSITION ANNEALS

I. INTRODUCTION

Transparent conducting oxides (TCOs) exhibit a unique mix of properties – high electrical conductivity approaching that of metals and high transmittance (>80%) in the visible region of the electromagnetic spectrum. TCOs are widely used in the optoelectronic industry for flat panel displays and solar cells *etc*. [5-1, 2]. To achieve metallic conductivity with TCOs without significant loss in transmittance, TCO-metal-TCO thin films have been studied in the past [5-3 – 5-5]. Studies have been done with silver as the embedded metal layer due to its low resistivity [5-6 – 5-10]. Deposition conditions and the thickness of the metal layer significantly influence the resulting optical and electrical properties [5-11, 12]. The embedded metal layer should be uniform, thin and continuous for high transmittance. Formation of isolated Ag islands leads to increased resistivity as well as decreased optical transmittance due to light scattering [5-10]. Among the TCOs, amorphous indium gallium zinc oxide (IGZO) is a promising candidate due to its high mobility and high transmittance [5-13 – 5-15]. It has been

successfully deposited on various substrates as glass [5-15] and polyethylene terephthalate (PET) [5-13] using co-sputtering [5-14] and pulsed laser deposition techniques [5-15]. The deposition and characterization of TCO-metal-TCO films have been extensively studied; however there is a lack of studies with IGZO as the TCO layer. Moreover, low-temperature microwave anneals have been shown to induce similar effects as thermal anneals [5-16]. However, the microwave anneals often allow the similar results to occur at lower temperatures. This fact makes microwave processing ideal for flexible electronics and photovoltaics. To this date, the use of low-temperature microwave processing of TCO-metal-TCO films has not been explored. This letter reports the fabrication of IGZO/Ag/IGZO multilayer structures with the highest conductivity and transmittance for optoelectronics applications. Further improvement in the transmittance is also investigated using susceptor-assisted microwave anneals.

II. EXPERIMENTAL

IGZO thin films were deposited by RF magnetron sputtering onto glass substrates using argon gas at 10 mTorr at 100 W power. Silver was deposited by DC magnetron sputtering at 10 mTorr and 40 W. Each of the top and bottom IGZO layers was approximately 25 nm thick; while, the silver layer thickness was varied between 5 and 10 nm. Bare IGZO layers without any silver were also deposited

under identical conditions for comparison of properties. Rutherford backscattering spectrometry (RBS) was used for determining the film thicknesses using the RUMP computer simulation program [5-17]. Silicon witness substrates were used for the ease of running RUMP simulations on the multilayer structures. The sample was rotated by 60 degrees with respect to the He^{++} beam so as to increase the signal from the sandwiched metal layer. Inspection of the microstructure was done using cross-section transmission electron microscopy (XTEM) using a Philips CM200-FEG TEM at an operating voltage of 200 kV. Defect contrast was enhanced using 220 bright-field and dark-field imaging. TEM samples were prepared using a FEI835 focused-ion beam tool with a gallium ion-source.

Carrier concentration and mobility were measured by Hall measurements employing the van der Pauw configuration on the Ecopia HMS 3000. Sheet resistance was measured by a four-point probe equipped with a 100 mA Keithley 2700 digital multimeter. The optical transmittance and reflectivity of the films were measured with an Ocean Optics double channel spectrometer (model DS200) in the wavelength range of 300-800 nm. Multilayer films with selected thicknesses of the Ag layer were annealed for 10 s in a single-frequency (2.45 GHz) cavity applicator microwave system, using a silicon carbide susceptor. A Raytek Compact MID series pyrometer was used to monitor the temperature. The peak temperature reached was 220 °C.

III. RESULTS

Figure 5-1 shows the backscattering spectrum and the corresponding RUMP simulation obtained on one of the various IGZO/Ag/IGZO multilayers deposited on a silicon witness substrate. From the simulation, the thickness of the sandwiched Ag layer in the particular multilayer structure was determined to be about 7.2 nm.

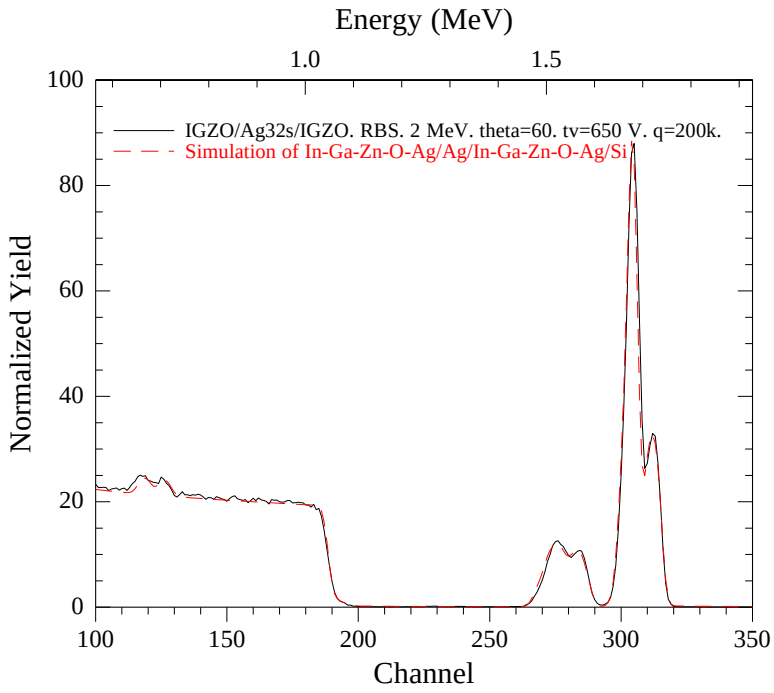

Fig. 5-1: RBS spectrum and the RUMP simulation on the IGZO/Ag/IGZO multilayer structure.

Figure 5-2 shows the XTEM micrographs of IGZO/Ag/IGZO multilayers obtained with varying thickness of the sandwiched metal layer. It is seen that the

multilayers with the thinnest Ag layers show discontinuities and island-like formations. This is similar to the observations by Sivaramakrishnan *et al.* [5-5] and Indluru *et al.* [5-10] in case of the ZnO/metal/ZnO and ITO/metal/ITO multilayers, respectively. As the thickness of the metal layer increases, the layer becomes more uniform and continuous.

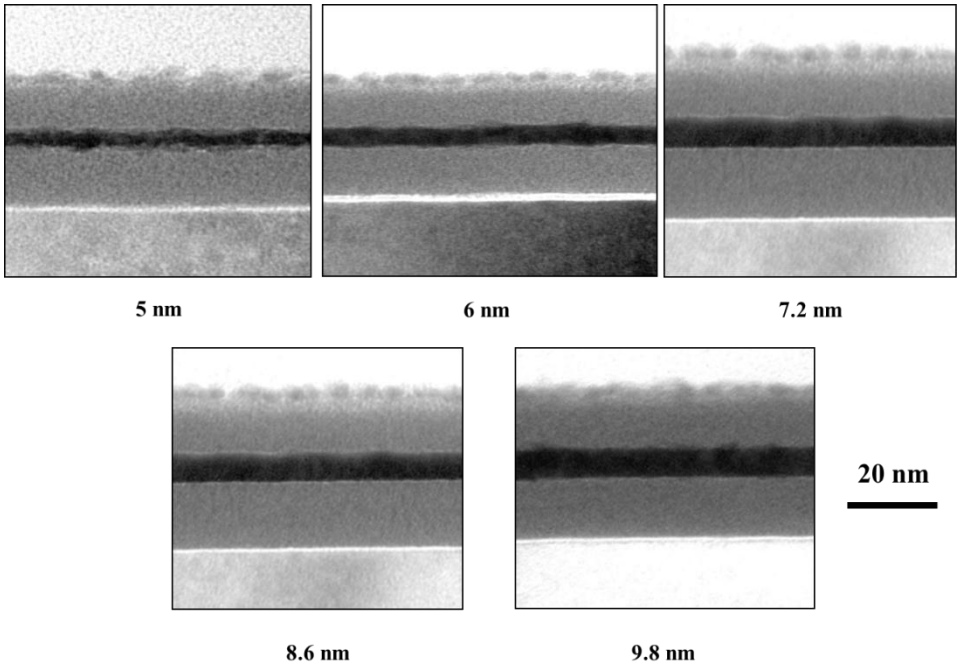

Fig. 5-2: XTEM micrographs of IGZO/Ag/IGZO multilayer structures with varying thickness of the sandwiched Ag layer.

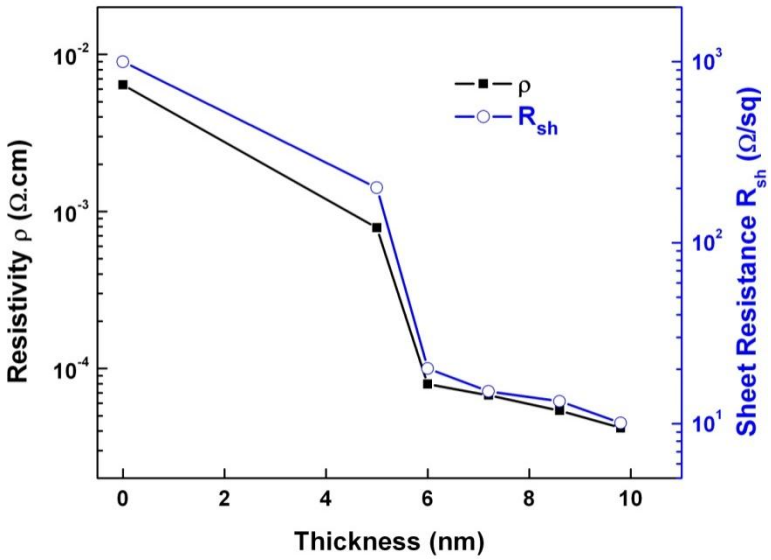

Fig. 5-3: Resistivity and sheet resistance of the IGZO/Ag/IGZO thin films as a function of silver layer thickness.

Figure 5-3 shows the dependence of the resistivity and sheet resistance of the IGZO/Ag/IGZO films on the Ag thickness. For the bare 60 nm thick IGZO films, the resistivity and sheet resistance values are 6.4×10^{-3} Ω-cm and 1000 Ω/sq., respectively. For the IGZO/Ag/IGZO multilayers, the resistivity drops to 4.2×10^{-5} Ω-cm at 9.8 nm of Ag thickness. The sheet resistance decreases from 1000 Ω/sq. to 10.1 Ω/sq.

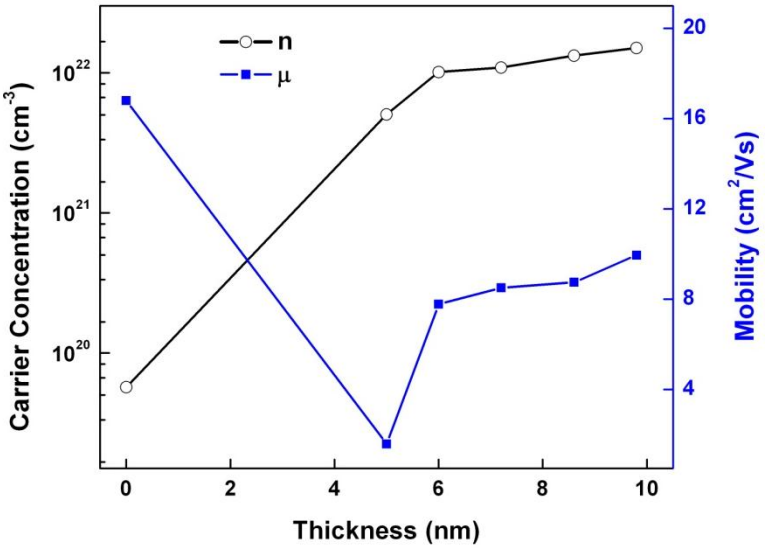

Fig. 5-4: Hall mobility and carrier concentration of the IGZO/Ag/IGZO thin films as a function of silver thickness.

Figure 5-4 shows the carrier concentration and mobility of the multilayer structures as a function of the thickness of the sandwiched Ag layer. It is seen that the incorporation of the metal layer significantly increases the carrier concentration of the multilayer system, and the carrier concentration steadily increases with increasing thickness of the Ag layer. The carrier mobility first shows a significant drop for very thin Ag layers and then increases with increasing Ag layer thickness.

Figure 5-5 shows optical transmittance spectra relative to the glass substrate for the IGZO/Ag/IGZO thin films for different Ag thicknesses. The transmittance of bare IGZO films is about 90% over the visible range of wavelengths. With the

silver mid-layers, T_{avg} drops to between 83% and 88%. Haacke [5-18] proposed a figure of merit (FOM) for TCO as $\frac{T_{avg}^{10}}{R_s}$; where T_{avg} is the average optical transmittance and R_s is the sheet resistance. To determine the Haacke FOM, the value of T_{avg} was calculated as [5-5]:

$$T_{avg} = \frac{\int V(\lambda)T(\lambda)d\lambda}{\int V(\lambda)d\lambda} \tag{5-1}$$

where $T(\lambda)$ is the transmittance and $V(\lambda)$ is the photopic luminous efficiency function defining the standard observer for photometry [5-19]. The figures of merit for the 5, 6, 7.2, 8.6 and 9.8 nm films were 7.9×10^{-4}, 1.6×10^{-2}, 1.7×10^{-2}, 1.67×10^{-2}, and 1.64×10^{-4} Ω^{-1}, respectively. The best figure of merit is obtained for the thinnest continuous Ag layer at thickness 7 nm.

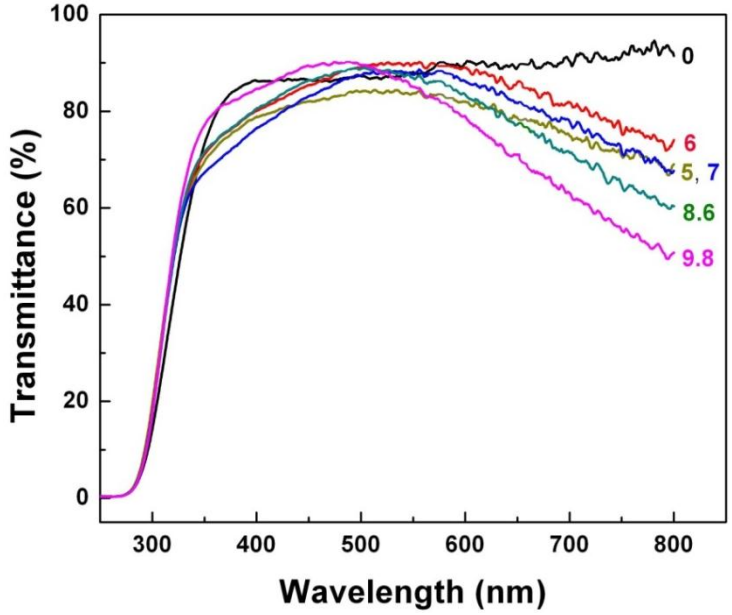

Fig. 5-5: UV-Vis Transmittance spectra relative to the glass substrate for the IGZO/Ag/IGZO thin films.

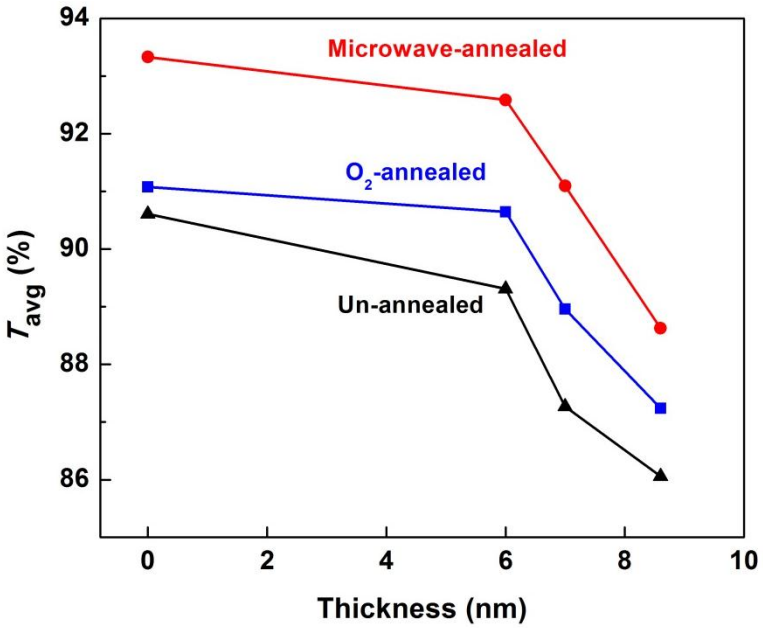

Fig. 5-6: Average transmittance (T_{avg}) for IGZO/Ag/IGZO thin films with varying silver thickness, before and after microwave annealing for 10 s and furnace-annealed in oxygen environment at 150 °C.

Figure 5-6 shows the effect of susceptor-assisted microwave annealing for 10 s and furnace annealing in oxygen environment for 2 hrs at 150 °C on T_{avg} for IGZO/Ag/IGZO multilayers for select thicknesses of Ag mid-layer. In both cases, T_{avg} shows an increment, with the microwave-anneals resulting in a higher Tavg than the corresponding oxygen-anneals. The T_{avg} for the un-annealed and annealed samples decreases with increasing Ag layer thickness.

IV. DISCUSSION

In this study, IGZO/Ag/IGZO multilayer structures are fabricated, characterized and their optical performance further improved by low-temperature annealing. The fabrication has been achieved at room-temperature using RF and DC sputtering, making it a suitable route for flexible substrates in addition to being a cost-effective and scalable process. Complete physical, electrical and optical characterization has been carried out. The optical performance of the multilayers is seen to further improve upon subjecting them to microwave-anneals and furnace-anneals in oxygen environment at 150 °C.

The reduction in resistivity can be understood by examination of the change in carrier concentration and mobility as shown in Fig. 5-4. The carrier concentration increases with increased thickness. The carrier concentration of bare IGZO is

about 5.7×10^{19} cm^{-3}. With a 9.8 nm Ag mid-layer, the carrier concentration is increased by nearly three orders of magnitude to 1.5×10^{22} cm^{-3}. As noted by Indluru *et al.*, the majority of the conduction thus happens through the sandwiched metal layer [5-10]. The carrier mobility for IGZO/3 nm Ag/IGZO is a low 1.6 $cm^2/V\,s$; while, the carrier concentration (5×10^{21} cm^{-3}) is two orders of magnitude higher than for bare IGZO films. The behavior shown by the carrier mobility is a peculiar trend. For the multilayer with the thinnest Ag layer, the metal layer is discontinuous with island-like formations as seen from Fig. 5-2. This discontinuous nature of the metal layer leads to a significant drop in the carrier mobility. The mobility then increases as the thickness of the metal layer increases. The work function of silver (ϕ = 4.5 eV) is smaller than that of IGZO (ϕ = 5 eV) [5-20, 21]. As a result, an Ohmic contact is formed at the metal-TCO interface with an accumulation of majority carriers in the IGZO layer. There is significant injection of carriers into the IGZO layer due to the difference in the work functions. This results in the substantial increase in conductivity of the multilayer structure even with 5 nm of silver mid-layer. However at this low Ag thickness, the IGZO/Ag/IGZO structure has much lower mobility than the bare IGZO films (Fig. 5-4) indicating that most of the current passes through the IGZO layer with the Ag islands acting as scattering sites that reduce the mobility. This is similar to the observation by Sivaramakrishnan and Alford in the case of ZnO/Cu/ZnO multilayer structures [5-4]. Further increases in the thickness of the

Ag mid-layer results in near-continuous metal layer formation as indicated by the increase in carrier concentration. At these thicknesses, the Ag mid-layer conducts a significant current. The net mobility is a result of the low mobility in the IGZO layer and the higher mobility in the discontinuous silver layer. At about 6 nm Ag thickness, the carrier concentration reaches the 1×10^{22} cm^{-3} range and suggests continuous Ag layer formation. For thicker Ag layers, most of the current passes through the low resistivity silver layer. Initially, the low mobility can be explained by high interface scattering from the thin Ag layer; but it gradually increases with increasing Ag thickness.

Silver particles of size less than a tenth of the wavelength of the light are known to absorb light by Mie resonance, with the resonant wavelength showing a blueshift with decreasing particle size [5-22]. Thus, the absorption in the silver films used in this study is mainly by Mie resonance in which the electrons can be treated as bound plasma oscillating at the plasma resonance frequency which lies in the UV region [5-23]. As seen in Fig. 5-3, transmittance at shorter wavelengths decreases as silver thickness increases up to 7 nm which can be explained by discontinuous Ag films causing increased scattering losses. Beyond this the transmittance increases with increasing Ag mid-layer thickness as the metal layers become continuous. In the red wavelengths, the scattering losses lead to reduced transmittance for 5 nm thick Ag layer and increases as the films start to become

continuous. Further increase in Ag mid-layer thickness leads to decreasing transmittance. The optical transmittance results support the conclusion that the Ag layer becomes continuous at a thickness greater than 6 nm and agrees with the conduction behavior.

As the thin films are microwave-annealed in air, the concentration of doubly-charged oxygen vacancies reduces according to $\frac{1}{2} O_{2(g)} + V^{\cdot\cdot}_{o} + 2 e^{-} \rightarrow O_{o}^{x}$. The reduced oxygen vacancy concentration leads to reduced carrier concentration in the IGZO layers and subsequently increased transmittance due to lower absorption by the free carriers, which dominates at longer wavelengths [5-24]. The sheet resistance of the annealed samples with Ag mid-layer was observed to be the same before and after the annealing. Since majority of the current passes through Ag mid-layers, reduced carrier concentration in IGZO layers is not seen to affect the overall conductivity of the multilayer structure. The confirmation of the role of oxygen vacancies in the optical absorption is obtained through the furnace-annealing of the IGZO/Ag/IGZO multilayer structures in oxygen environment at 150 °C. The oxygen-anneals also result in an improvement in the average transmittance. Higher degree of improvement in the case of microwave anneals could be explained by higher temperatures achieved during microwave anneals. Moreover, the microwave anneals are very short (10 s) as compared to the oxygen anneals (2 hrs). Longer anneals avoid any kinetic barrier in the

activation of dopants and hence may result in higher level of dopant activation, which leads to a smaller reduction in carrier concentration as compared to very short anneals and hence a smaller improvement in the optical performance. IGZO layers without any sandwiched metal layer have been used as a control in this study, helping to confirm the role of oxygen vacancies in the improvement in optical transmittance upon annealing.

V. CONCLUSION

In conclusion, high conductivity IGZO/Ag/IGZO films with high transmittance were obtained. For multilayers with 7 nm Ag layers, the carrier concentration was 1×10^{22} cm^{-3} and resistivity was 6.7×10^{-5} Ω-cm, while still achieving T_{avg} at 87%, resulting in FOM of 1.7×10^{-2} Ω^{-1}. Low resistivity and high T_{avg} were obtained when the Ag layer thickness corresponds to the initial formation of a continuous metal layer. The multilayers were subsequently microwave-annealed which resulted in decrease in the oxygen vacancy concentration thereby reducing the free carrier absorption and improving the T_{avg} . This was confirmed by furnace-annealing the films in oxygen environment.

Chapter 6

SUMMARY AND FUTURE WORK

I. SUMMARY OF RESEARCH WORK

In this study, improved electrical and optical properties upon thermal and microwave processing of mixed-oxide semiconductors is reported. First, arsenic-doped silicon was used as a model system to understand susceptor-assisted microwave annealing. Arsenic implanted silicon samples were microwave-processed assisted by SiC susceptors, to temperatures required for solid phase epitaxy in silicon. The susceptor-assisted heating allowed attainment of temperatures above 700 ^{o}C and thereby reducing processing times as well as achieving near-complete electrical activation of the dopants. Different microwave loss mechanisms were responsible for the conversion of microwave power to heat in the experimental set-up: dipole polarization losses in the susceptor in the low-temperature range and Ohmic conduction losses in the ion-implanted silicon in the high-temperature range. Sample surface temperatures ranged 620-730 ^{o}C. The characteristic shape of the temperature profile was explained. Microwave processing of arsenic-implanted silicon, for 40-100 s, resulted in the repair of nearly all radiation damage as monitored by sheet resistance and RBS. The process of dopant activation was observed to not be kinetically limited above a

surface temperature of 680 ºC. Moreover, electrical activation of the dopants was achieved without any significant diffusion of the dopants deeper into the substrate, which is advantageous for the processing of modern field-effect transistors.

Mixed oxide semiconductor films of indium zinc oxide (IZO) and indium gallium zinc oxide (IGZO) were deposited by room-temperature RF sputtering on flexible polymer substrates. Thermal annealing in different environments - air, vacuum, oxygen and forming gas was done. Electrical and optical characterization was carried out before and after annealing.

For the a-IZO films on PEN, an approximately 62-fold increase in the Haacke FOM was achieved by annealing the films in air at 150 ºC for 6 hrs. Difference in electrical performance of films annealed in different environments resulted from change in the concentration of oxygen vacancies. It was demonstrated that the degradation in the electrical properties upon exposure to oxidizing environment can be reversed by employing further vacuum anneals. The degree of reversal in the degradation in electrical properties of the thin films upon annealing in oxygen was assessed by subjecting samples to subsequent vacuum anneals. The agreement between the measured values of carrier mobility and the values

calculated using a model showed that the mobility was influenced by structural defects at low carrier concentrations.

Amorphous IGZO thin films of the highest transmittance reported in literature were deposited onto flexible polymer substrates at room temperature. The films were annealed in vacuum, air, and oxygen to enhance electrical and optical performance. Electrical and optical characterization was done before and after annealing. A partial reversal of the degradation in electrical properties upon annealing in oxygen was achieved by subjecting the films to subsequent vacuum anneal. A model based on film texture and structural defects which showed close agreement between the measured and calculated carrier mobility values.

To further increase the conductivity of the IGZO films, Ag midlayers of various thicknesses were embedded between two IGZO layers. Optical performance of the multilayer structures was improved by susceptor-assisted microwave annealing without compromising on their electrical conductivity. The post-processing of the films in different environments was used to develop an understanding of mechanisms of carrier generation, transport and optical absorption. The microwave and furnace anneals resulted in decrease in the oxygen vacancy concentration thereby reducing the free carrier absorption and improving the T_{avg}. This was confirmed by furnace-annealing the films in oxygen

environment. The difference in the extent of improvement in the optical transmission upon annealing by the two methods was explained by the longer duration of oxygen anneals.

This study establishes IGZO as a viable transparent conductor, which can be deposited at room-temperature and processed by thermal and microwave annealing for applications in flexible electronics and optoelectronics. It can also be used as the highly transparent TCO component of TCO/metal/TCO multilayer structures offering very high conductivity and optical transmittance.

II. FUTURE WORK

In the present study, thermal and microwave processing of thin film samples has been carried out. For the microwave processing of materials – both covalent semiconductors like silicon and amorphous transparent conducting oxides like IGZO, it may be attempted to process larger samples. This may be used for investigating into any non-uniformities resulting from the microwave anneals. More number of temperature probes may be used. Electrical properties like sheet resistance may be measured at various points on a larger wafer to map the non-uniformity in the single-frequency microwave cavity applicator. As a control, a wafer annealed in a furnace or a hot plate may be used. Moreover, use of

multiple-frequency microwave cavity applicators may be employed to obtain better uniformity and possibly to further hasten the processing. In this study, the microwave anneals have been carried out in ambient conditions. Various other environments like inert gases (e.g. argon), oxidizing environments (e.g. oxygen) and reducing environments (e.g. forming gas) may be used and their effect studied on the properties of materials being processed.

Amorphous thin films of IZO and IGZO have been deposited on flexible polymer substrate PEN. The effect of deposition conditions and annealing on the emissivity of these the mixed oxide semiconductor thin films may be studied and their emissivities compared to the existing commercial low-emissivity (*'low-e'*) coatings. Control of oxygen vacancies during the deposition may be achieved by changing the proportion of oxygen in the sputter gas mixture. Obtaining lower carrier concentrations may be useful while attempting to use the amorphous oxides as channel layers in transparent thin film transistors (TTFTs). The highly transparent and highly conducting IGZO thin films achieved in this study may be used as electrodes in organic solar cells. If integrated with p-type TCOs, they could be used to form various components of transparent circuits such as transparent p-n junction diodes and transistors. IGZO films deposited on PEN may be integrated into organic light emitting diode (OLED) displays.

For the IGZO/metal/IGZO multilayer structures, different metals may be tried and the relative electrical and optical performance of the multilayers may be studied. Some choices for the metal layer are gold and copper. Recently, there has been a tremendous recent interest in graphene as one of the materials for optoelectronics. The highly transparent IGZO films achieved in the present work may be combined with the highly conductive graphene to form high-performance multilayer structures.

Amorphous IGZO thin films may also be deposited by a sol-gel route and its stability and manufacturability compared with the RF sputtering at room temperature. Also, mechanical properties of the IGZO thin films on flexible polymer substrates like PEN and PET may be studied and compared. Investigation of the effects on the electrical and optical properties of the IGZO films upon mechanical stress and electrical stress may be carried out. An interesting study may be to explore the behavior of TCO films under simultaneous application of mechanical and electrical stress, closely simulating on-field situations. Also, the films deposited on polymer substrates may be exposed to humidity and temperature and its effect on their electrical and optical performance as well as mechanical stability may be investigated. Temperature and humidity-controlled chambers (T&H chambers) may be used for the same.

REFERENCES

Chapter 1:

[1-1] Manoj Gupta, Wong Wai Leong, Eugene, **Microwaves and Metals**, John Wiley and Sons (Asia) Pte Ltd. (2007).

[1-2] R. E. Newnham, S. J. Jang, Ming Xu, Frederick Jones, Ceramic Transactions **21**, 51 (1991).

[1-3] D. E. Clark, W. H. Sutton, Annu. Rev. Mater. Sci. **26**, 299 (1996).

[1-4] Yu V. Bykov, K. I. Rybakov, V. E. Semenov, J. of Phys. D: Appl. Phys. **34,** R55 (2001).

[1-5] David C. Paine, Hyo-Young Yeom, Burag Yaglioglu, **Transpardent Conducting Oxide Materials and Technology**, Flexible Flat Panel Displays Ed. Gregory Crawford (2005).

[1-6] A. G. MacDiarmid, Synthetic Metals **125**, 11 (2002).

[1-7] G. J. Exarhos, X.–D. Zhou, Thin Solid Films **515**, 7025 (2007).

[1-8] G. Haacke, J. of App. Phys. **47**, 4086 (1976).

[1-9] Arun Suresh, Patrick Wellenius, Anuj Dhawan, John Muth, App. Phys. Lett. **90**, 123512 (2007).

[1-10] H. Hosono, J. Non-Cryst. Solids **352**, 851 (2006).

[1-11] K. Nomura, T. Kamiya, H. Ohta, T. Uruga, M. Hirano, H. Hosono, Phys. Rev. B **75**, 035212 (2007).

[1-12] Burag Yaglioglu, Yen-Jung Huang, Hyo-Young Yeom and David C. Paine, Thin Solid Films **496**, 89 (2006).

Chapter 2:

[2-1] *International Technology Roadmap for Semiconductors* (Semiconductor Industry Association) (http://www.itrs.net).

[2-2] D. K. Schroder, Semiconductor Material and Device Characterization, John Wiley & Sons, Hoboken, New Jersey (2006).

[2-3] R. F. Pierret, Semiconductor Device Fundamentals, Addison-Wesley, Reading, (1996).

[2-4] J. W. Mayer and S. S. Lau, Electronic Materials Science: For Integrated Circuits in Si and GaAs, Macmillan Publishing Company, New York, NY (1990).

[2-5] K. N. Tu, J. W. Mayer, and L. C. Feldman, Electronic Thin Film Science, Macmillan Publishing Company, New York, NY, (1992).
[2-6] J. D. Plummer, M. D. Deal, P. B. Griffin, Silicon VLSI Technology: Fundamentals, Practice and Modeling, Prentice Hall, Upper Saddle River, NJ (2000).
[2-7] A. V. Rzhanov, N. N. Gerasimenko, S. V. Vasil'ev, and V. I. Obodnikov, Sov. Tech. Phys. Lett. **7**, 521 (1981).
[2-8] S.–L. Zhang, R. Buchta, and D. Sigurd, Thin Solid Films **246**, 151 (1994).
[2-9] H. Zohm, E. Kasper, P. Mehringer, and G. A. Müller, Microelec. Eng. **54**, 247 (2003).
[2-10] E. L. Pankratov, J. Appl. Phys. Lett. **103**, 064320 (2008).
[2-11] D. C. Thompson, H. C. Kim, T. L. Alford, and J. W. Mayer, Appl. Phys. Lett. **83**, 3918 (2003).
[2-12] D. C. Thompson, T. L. Alford, J. W. Mayer, T. Hochbauer, M. Nastasi, S. S. Lau, N. David Theodore, K. Henttinen, llkka Suni, and Paul K. Chu, Appl. Phys. Lett. **87**, 224103 (2005).
[2-13] T. L. Alford, D. C. Thompson, J. W. Mayer, N. David Theodore, J. App. Phys. **106**, 114902 (2009).
[2-14] T. Sato, Jpn. J. Appl. Phys. **6**, 339 (1967).
[2-15] L. R. Doolittle, Nuc. Inst. & Meth. Phys. Res. **B9**, 344 (1985).
[2-16] Bo Lojek, 16th IEEE International Conference on Advanced Thermal Processing of Semiconductors (2008).
[2-17] R. E. Newnham, S. J. Jang, Ming Xu, Frederick Jones, Ceramic Transactions **21**, (1991).
[2-18] W. H. Sutton, Am. Ceram. Soc. Bull. **68**, 376 (1989).
[2-19] J. M. Kowalski, J. E. Kowalski, Bo Lojek, 15th IEEE International Conference on Advanced Thermal Processing of Semiconductors (2007).
[2-20] David E. Clark, Diane C. Folz, Jon K. West, Materials Science and Engineering **A287**, 153 (2000).
[2-21] R. B. Fair, J. App. Phys. **51**, 5828 (1980).
[2-22] D. Mathiot, J. C. Pfister, J. App. Phys. **55**, 3518 (1984).
[2-23] H. Zohm, E. Kasper, P. Mehringer, G. A. Muller, Microelectronic Engineering **54**, 247-253 (2000).
[2-24] R. B. Fair, Diffusion and Ion Implantation in Gary E. McGuire Ed. Semiconductor Materials and Process Technology, Noyes Publication (1998).
[2-25] Leonard C. Feldman, James W. Mayer, S. Thomas Picraux, Materials Analysis by Ion Channeling, Academic Press 1982.
[2-26] B. Swaminathan, K. C. Saraswat, R. W. Dutton, Appl. Phys. Lett., **40**(9) 1982.

[2-27] M. D. Giles, J. Electrochem. Soc. **138**, 1160 (1991).
[2-28] L. Pelaz, G. H. Gilmer, M. Jaraiz, S. B. Herner, H.-J. Gossmann, D. J. Eaglesham, G. Hobler, C. S. Rafferty, J. Barbolla, Appl. Phys. Lett. **73**, 1421 (1998).

Chapter 3:

[3-1] T. Minami, Semicond. Sci. Technol. **20**, S35 (2005).
[3-2] K. Nomura, A. Takagi, T. Kamiya, H. Ohta, M. Hirano, H. Hosono, Jap. J. of App. Phys. **45**, 4303 (2006).
[3-3] W. A. MacDonald, J. Mater. Chem. **14**, 4 (2004).
[3-4] W. A. McDonald, K. Rollins, R. Eveson, K. Rakos, B. A. Rustin, M. Handa, Materials Research Society Symposium Proceedings **769**, 283 (2003).
[3-5] G. Haacke, J. of App. Phys. **47**, 4086 (1976).
[3-6] D. C. Payne, Hyo-Young Yeom, Burag Yaglioglu, *Flexible Flat Panel Displays* ed. G. P. Crawford, John Wiley and Sons Ltd., (2005).
[3-7] H. Han, Y. Zoo, S. K. Bhagat, J. S. Lewis, T. L. Alford, J. of App. Phys. **102**, 063710 (2007).
[3-8] Y. S. Jung, J. Y. Seo, D. W. Lee and D. Y. Jeon, Thin Solid Films **445**, 63 (2003).
[3-9] W. Lim, D. P. Norton, J. H. Jang, V. Craciun, S. J. Pearton, F. Ren, Appl. Phys. Letts. **92**, 122102 (2008).
[3-10] K. Sivaramakrishnan and T. L. Alford, Appl. Phys. Letts. **96**, 201109, 2010.
[3-11] V. Bhosle, A. Tiwari, and J. Narayan, Appl. Phys. Lett. **88**, 032106 (2006).
[3-12] N. Ito, Y. Sato, P. K. Song, A.Kaijio, K. Onoue, Y. Shigesato, Thin Solid Films **496**, 99 (2006).
[3-13] W. Lim, Y.-L. Wang, F. Ren, D. P. Norton., I. I. Kravchenko, J. M. Zavada, S. J. Pearton, Electrochem. and Solid-State Letts. **10**, H267 (2007).
[3-14] Y.-S. Park, H.-K. Kim, S.-W. Jeong, W.-J. Cho, Thin Solid Films **518**, 3071 (2010).
[3-15] E. L. Kim, S. K. Jung, S. H. Sohn, D. K. Park, J. Phys. D: Appl. Phys. **40**, 1784 (2007).
[3-16] R. Martins, P. Barquinha, I. Ferreira, L. Pereira, G. Goncalves, E. Fortunato, J. of Appl. Phys. **101**, 044505 (2007).
[3-17] H. Ehrenreich and H. R. Philipp, Phys. Rev. **128**, 1622 (1962).
[3-18] R. Martins, P. Barquinha, A. Pimentel, L. Pereira and E. Fortunato, Phys. Stat. Sol. (a) **202**, R95 (2005).

[3-19] H. M. Ng, D. Doppalapudi, T. Moustakas, Appl. Phys. Letts. **73**, 821 (1998).

Chapter 4:

[4-1] R. L. Hoffman, B. J. Norris, and J. F. Wager, Appl. Phys. Lett. **82**, 733 (2003).
[4-2] P. Barquinha, E. Fortunato, A. Goncalves, A. Pimentel, A. Marques, L. Pereira, and R. Martins, Superlattices Microstruct. **39**, 319 (2006).
[4-3] R. Navamathavan, E.-J. Yang, J.-H. Lim, D.-K. Hwang, J.-Y. Oh, J.-H. Yang, J.-H. Jang, and S.-J. Park, J. Electrochem. Soc. **153**, G385 (2006).
[4-4] R. E. Presley, C. L. Munsee, C.-H. Park, D. Hong, J. F. Wager, and D. A. Keszler, J. Phys. D **37**, 2810 (2004).
[4-5] C. G. Granqvist, A. Hultaker, Thin Solid Films **411**, 1 (2005).
[4-6] N. L. Dehuff, E. S. Kettenring, D. Hong, H. Q. Chiang, J. F. Wager, R. L. Hoffman, C.-H. Park, and D. A. Keszler, J. Appl. Phys. **97**, 064505 (2005).
[4-7] H. Q. Chiang, J. F. Wager, R. L. Hoffman, J. Jeong, and D. A. Keszler, Appl. Phys. Lett. **86**, 013503 (2005).
[4-8] K. Nomura, H. Ohta, A. Takagi, T. Kamiya, M. Hirano, and H. Hosono, Nature **432**, 488 (2004).
[4-9] J. F. Wager, Science **300**, 1245 (2003).
[4-10] K. Nomura, H. Ohta, K. Ueda, T. Kamiya, M. Hirano, and H. Hosono, Science **300**, 1269 (2003).
[4-11] K. Nomura, T. Kamiya, H. Ohta, T. Uruga, M. Hirano, Hideo Hosono, Phys. Rev. B **75**, 035212 (2007).
[4-12] H. Hosono, N. Kikuchi, N. Ueda, H. Kawazoe, J. Non-Cryst. Solids **198**, 165 (1996).
[4-13] H. Hosono, M. Yasukawa, H. Kawazoe, J. Non-Cryst. Solids **203**, 334 (1996).
[4-14] H. L. Hartnagel, A. L. Dawar, A. K. Jain, C. Jagadish, *Semiconductor Transparent Thin Films,* Institute of Physics Publishing, Bristol (1995).
[4-15] H. J. Chang, K. M. Huang, C. H. Chu, S. F. Chen, T. H. Huang, and M. C. Wu, ECS Transactions **28**, 137 (2010).
[4-16] K. Inoue, K. Tominaga, T. Tsuduki, M. Mikawa, T. Moriga, Vacuum **83**, 552 (2009).
[4-17] K. Sivaramakrishnan and T. L. Alford, Appl. Phys. Letts. **94**, 052104 (2009).

[4-18] A. Suresh, P. Gollakota, P. Wellenius, A. Dhawan, J. F. Muth, Thin Solid Films **516**, 1326 (2008).
[4-19] G. Haacke, J. of App. Phys. **47**, 4086 (1976).
[4-20] K. Sivaramakrishnan and T. L. Alford, Appl. Phys. Letts. **96**, 201109 (2010).
[4-21] H. Ehrenreich and H. R. Philipp, Phys. Rev. **128**, 1622 (1962).
[4-22] R. Martins, P. Barquinha, I. Ferreira, L. Pereira, G. Goncalves, E. Fortunato, J. of Appl. Phys. **101**, 044505 (2007).
[4-23] D. C. Payne, Hyo-Young Yeom, Burag Yaglioglu, *Flexible Flat Panel Displays* ed. G. P. Crawford, (John Wiley and Sons Ltd., 2005).
[4-24] R. Martins, P. Barquinha, A. Pimentel, L. Pereira and E. Fortunato, Phys. Stat. Sol. (a) **202**, R95 (2005).

Chapter 5:

[5-1] C. G. Granqvist and A. Hultaker, Thin Solid Films **411**, 1 (2002).

[5-2] R. G. Gordon, MRS Bull. **25**, 52 (2000).

[5-3] C. Guillen and J. Herrero, Sol. Energy Mater. Sol. Cells **92**, 938 (2008).

[5-4] K. Sivaramakrishnan and T. L. Alford, Appl. Phys. Letts. **94**, 052104 (2009).

[5-5] K. Sivaramakrishnan and T. L. Alford, Appl. Phys. Lett. **96**, 201109 (2010).

[5-6] S. Kim, Y. Moon, D. Moon, M. Hong, Y. Jeon, and J. Park, J. Korean Phys. Soc. **49**, 1256 (2006).

[5-7] M. Bender, W. Seelig, C. Daube, H. Frankenberger, B. Ocker and J. Stollenwerk, Thin Solid Films **326**, 72 (1998).

[5-8] D. R. Sahu, S. Lin, and J. Huang, Applied Surface Science **252**, 7509 (2006).

[5-9] Jin-A Jeong, Yong-Seok Park and Han-Ki Kim, J. Appl. Phys. **107**, 023111 (2010).

[5-10] A. Indluru and T. L. Alford, J. Appl. Phys. **105**, 123528 (2009).

[5-11] M. Kawamura, Y. Abe, and K. Sasaki, Thin Solid Films **515**, 540 (2006).

[5-12] M. K. Sinha, S. K. Mukherjee, B. Pathak, R. K. Paul, and P. K. Barhai, Thin Solid Films **515**, 1753 (2006).

[5-13] K. Nomura, H. Ohta, A. Takagi, T. Kamiya, M. Hirano, and H. Hosono, Nature **432**, 488 (2004).

[5-14] H. J. Chang, K. M. Huang, C. H. Chu, S. F. Chen, T. H. Huang, and M. C. Wu, ECS Transactions **28**, 137 (2010).

[5-15] K. Inoue, K. Tominaga, T. Tsuduki, M. Mikawa, T. Moriga, Vacuum **83**, 552 (2009).

[5-16] R.N.P. Vermuri, N. D. Theodore, W. Chen, S.S. Lau, and T.L. Alford, *accepted to* Journal of Applied Physics (2011).

[5-17] L. R. Doolittle, Nucl. Instrum. Methods Phys. Res. B **9**, 344 (1985).

[5-18] A. G. Milnes and D. L. Feucht, *Heterojunciton and Metal-Semiconductor Junctions* (Academic, New York, 1972).

[5-19] B. D. Ahn, W. H. Jeong, H. S. Shin, D. L. Kim, H. J. Kim, J. K. Jeong, S.-H. Choi, M.-K. Han, Electrochemical and Solid-State Letts. **12**, H430 (2009).

[5-20] G. Haacke, J. Appl. Phys. **47**, 4086 (1976).

[5-21] W. G. Driscoll and W. Vaughan, *Handbook of Optics* (McGraw-Hill, USA, 1978).

[5-22] A. Liebsch, Phys. Rev. B. **48**, 11317 (1993).

[5-23] J. Tiggesbäumker, L. Köller, K.-H. Meiwes-Broer, A. Liebsch, Phys. Rev. A. **48**, R1749 (1993).

[5-24] H. Ehrenreich and H. R. Philipp, Phys. Rev. **128**, 1622 (1962).